②

R and D CENTER LABORATORY

TECHNICAL REPORT

NO. **13004**

THEORETICAL AND EXPERIMENTAL INVESTIGATION
OF MECHANICALLY FASTENED COMPOSITES
JULY 84

Contract No DAAE07-82-K-4002

DTIC
SELECTED
MAR 6 1985
B

Gary Cloud
David Sikarskie
Enayat Maha...
Pedro He...
Michigan State University
E. Lansing, MI   48823-1226

by

20000804009

**U.S. ARMY TANK-AUTOMOTIVE COMMAND
RESEARCH AND DEVELOPMENT CENTER
Warren, Michigan 48090**

NOTICES

This report is not to be construed as an official Department of the Army position.

Mention of any trade names or manufacturers in this report shall not be construed as an official indorsement or approval of such products or companies by the US Government.

Destroy this report when it is no longer needed. Do not return it to the originator.

REPORT DOCUMENTATION PAGE

1a. REPORT SECURITY CLASSIFICATION Unclassified	1b. RESTRICTIVE MARKINGS None
2a. SECURITY CLASSIFICATION AUTHORITY	3. DISTRIBUTION / AVAILABILITY OF REPORT Approved for public release distribution unlimited
2b. DECLASSIFICATION / DOWNGRADING SCHEDULE	

4. PERFORMING ORGANIZATION REPORT NUMBER(S)	5. MONITORING ORGANIZATION REPORT NUMBER(S) TACOM T.R. #13004

6a. NAME OF PERFORMING ORGANIZATION Michigan State University	6b. OFFICE SYMBOL (If applicable)	7a. NAME OF MONITORING ORGANIZATION TACOM AMSTA-RCKM

6c. ADDRESS (City, State, and ZIP Code) Dept. of Met. Mech. & Mat. Sci. Michigan State University E. Lansing, MI 48824-1226	7b. ADDRESS (City, State, and ZIP Code) TACOM Attn: AMSTA-RCKM Warren, MI 48090

8a. NAME OF FUNDING / SPONSORING ORGANIZATION Same as 7	8b. OFFICE SYMBOL (If applicable)	9. PROCUREMENT INSTRUMENT IDENTIFICATION NUMBER Contract DAAE07-82-K-4002

| 8c. ADDRESS (City, State, and ZIP Code) | 10. SOURCE OF FUNDING NUMBERS |

PROGRAM ELEMENT NO.	PROJECT NO.	TASK NO.	WORK UNIT ACCESSION NO.

11. TITLE (Include Security Classification)

Theoretical and Experimental Investigation of Mechanically Fastened Composites

12. PERSONAL AUTHOR(S)
Cloud, Gary; Sikarskie, David; Mahajerin, Enayat; and Herrera, Pedro

13a. TYPE OF REPORT Final	13b. TIME COVERED FROM 9/82 TO 9/83	14. DATE OF REPORT (Year, Month, Day) 1984 July	15. PAGE COUNT

16. SUPPLEMENTARY NOTATION

17. COSATI CODES			18. SUBJECT TERMS (Continue on reverse if necessary and identify by block number)
FIELD	GROUP	SUB-GROUP	

19. ABSTRACT (Continue on reverse if necessary and identify by block number)

The mechanics of fasteners in composites were studied in a combined experimental-theoretical research program. The objectives were to gain fundamental insight into the stress-strain field near pin-type fasteners and to provide guidance to designers responsible for the selection and sizing of fasteners. The primary experimental method utilizes Moiré interference with optical Fourier processing of grid photoplates. A new technique using optical interference to generate gratings in three directions was developed to gain a factor of 10 in sensitivity. The constitutive properties of the material studied were measured. For the analytical work, a boundary element method (BEM) was developed, a compact and efficient computer code written, and the method compared with the finite-element method (FEM). For the problems investigated, the BEM is more efficient. The material used was fiber glass-epoxy laminate with woven fibers. The analytical and experimental forces were brought to bear on the problem of a loaded pin snugly fit in a hole. Results from the two approaches agreed well for the specific composite.

20. DISTRIBUTION / AVAILABILITY OF ABSTRACT ☒ UNCLASSIFIED/UNLIMITED ☐ SAME AS RPT. ☐ DTIC USERS	21. ABSTRACT SECURITY CLASSIFICATION
22a. NAME OF RESPONSIBLE INDIVIDUAL Avery H. Fisher	22b. TELEPHONE (Include Area Code) 313-574-5879 22c. OFFICE SYMBOL AMSTA-RSC

DD FORM 1473, 84 MAR   83 APR edition may be used until exhausted.
All other editions are obsolete.

PREFACE

The research described in this report was conducted at Michigan State University in the Department of Metallurgy, Mechanics and Materials Science and in the Center for Composite Materials and Structures. Investigators were Dr. Gary Cloud, Professor; Dr. David Sikarskie, Chairman; Dr. Enayat Mahajerin, Post-doctoral Student; and Mr. Pedro Herrera, Doctoral Candidate. Manuscript preparation was by Ms. Arlene Klingbiel.

3

This page left blank intentionally.

TABLE OF CONTENTS

This page left blank intentionally.

LIST OF FIGURES

LIST OF TABLES

This page left blank intentionally.

1.0. INTRODUCTION

1.1. Background

There has been a dramatic increase in the use of composite materials. The center of gravity of this growth has been in aerospace and defense-related industries. As composite material developments continue to increase, resulting in decreases in cost, use of these materials will naturally spread to other industries.

One of the attractive features of composites as opposed to metals is their ability to be molded into complex "final shape." Important advantages of this approach include requiring a minimum number of fasteners as well as being able to locate the necessary fasteners in regions of low stress. Because of cost, however, such elaborate design is usually possible only for sophisticated structures, e.g., military aircraft. While fastener problems are significant in these structures, it is expected that their importance will increase as composites usage spreads to less-sophisticated applications.

The fastening of composites poses some special problems. In the fastening of metals, normal metal plasticity acts as an "averaging" mechanism tending to relieve both high local stresses and uneven load distribution in fastener patterns. In general, composites are considerably more brittle, more sensitive to stress concentrations, and have much lower strain to failure. Fastener techniques which distribute bearing loads more evenly (reduce stress concentrations) result in higher-strength joints. Techniques which distribute bearing loads include fastener arrays, interference-fit fasteners, glued fasteners, and hybrid adhesive-mechanical joints. A typical example involves replacing load-aligned graphite fibers near the fastener hole with lower-modulus glass fibers. Stress concentration relief in the interference-fit fastener case is derived from a matrix "softening" in the vicinity of the hole. This softening is actually an inter-or intra-ply separation which can occur without fiber breakage.

1.2. Project Summary

The contractors conducted a one-year study of the mechanics of fasteners in composites. It should be noted that the analytical and experimental tools used in this study are fairly novel, particularly in the context of composite fastening, and in that sense are unique contributions in their own right. The theoretical effort concentrates on the extension of boundary element methods to determine stress-strain fields for complex multiply-connected and three-dimensional geometries with anisotropic materials. Experimental approaches include a Moire method involving high-resolution grating replication, Fourier optical processing of grating replicas, and digital data reduction.

This report describes the methodology developed for both the analytical and experimental studies. The techniques developed were used to determine

11

stresses and strains in the vicinity of a single-pin loose-fit lap joint in an actual glass-epoxy composite; these results are reported. The properties of the composite were measured so that theory and experiment could be compared. The comparison, which is described in Section 4.0, showed good agreement for the fundamental case studied.

While this one-year effort was successful in terms of methodology and results, it was viewed from the start by the researchers involved as the early steps in a more comprehensive research program. A unique aspect of this program is that the experimental and analytical techniques are simultaneously being developed and used by researchers in the same group. This work is necessary before systematic fabrication of structures from composites can be successful in engineering and economic terms. The effort is considerably enhanced by having the theoretical and experimental researchers together. Significant progress has been made after the close of the one-year contract because the contractors were committed to the ideas and the people involved. The researchers feel strongly that the major benefits will come from research yet to be done, and they suggest that continued support is appropriate for proper realization of the resources and personnel already developed.

2.0. ANALYTICAL DEVELOPMENT, RESULTS AND COMPARISON

2.1. Problem Statement

This section presents the analytical development of a boundary element formulation for calculating stresses and deformations in mechanically fastened composites. The purpose of this development results from the following observations. In a vast majority of the composites literature in which stress and/or deformation calculations are required, the finite element method (FEM) is used. This method is, of course, very powerful and has the advantage of access to well developed codes. It is not necessarily the most efficient numerical procedure, however. Numerous authors have shown (1)* that the boundary element method is, for certain classes of problems, considerably more efficient than the FEM. The main purpose of this section is to develop a boundary element method (BEM) code pertinent to a mechanically fastened composite structure. This code will then be directly compared with a current state-of-the-art FEM code to see if significant improvement in efficiency is possible. For comparative purposes both codes are run on the same computer, a Prime 250. In terms of problem selection for comparative purposes there are a number of possible boundary value problems to look at in the composite fastening area. Examples include multiple fasteners, interference fit fasteners, softening strips, etc. For this example, a simple lap joint, single pin, loose fit connector is considered, and results using both numerical methods are compared. If improvements can be shown in the simple case, it is reasonable to expect improvement in more complicated situations.

---

*Numbers in parenthesis refer to references given at the end of Section 4.0.

12

However, code development for the more complicated situations are covered under future proposed research. The next subsection will explain the BEM formulation. This is followed by the solution of some example problems and a comparison of BEM and FEM.

2.2. BEM Formulation

Let an anisotropic body (Figure 2-1) occupy a finite open plane region D bounded by a single smooth contour ∂D which admits a representation in the form $x_i = x_i(s)$. The parameter s is the length along ∂D from an arbitrary origin, and x_i are cartesian coordinates (see Figure 2-1). For the well-known mixed boundary value problem of anisotropic elastostatics:

$$S_{\alpha\beta\gamma\delta} u_{\gamma,\delta\beta} = 0 \quad \text{in } D$$

$$\sigma_{\beta\gamma} n_\gamma = \bar{t}_\beta \quad \text{on } \partial D_t \tag{1}$$

$$u_\beta = \bar{u}_\beta \quad \text{on } \partial D_u$$

$$\alpha,\beta,\gamma = 1,2 \quad \partial D = \partial D_t + \partial D_u$$

u_γ represents the displacement components, the comma denotes differentiation with respect to the arguments after the comma, $\sigma_{\beta\gamma}$ is a component of stress, t_β is the corresponding traction vector, n_γ is a component of the unit outward normal to the boundary ∂D, and $S_{\alpha\beta\gamma\delta}$ denotes the "stiffness tensor" for the material. To solve this problem by an indirect boundary element method, one can apply the initially unknown layer of body forces R_γ to the boundary of the embedded region and use the principle of superposition to obtain (2):

$$\sigma_{\alpha\beta}(\xi) = \int H_{\alpha\beta\gamma} (\xi,x')R_\gamma(x')ds \tag{2}$$

$$u_\beta(\xi) = \int U_{\beta\gamma} (\xi,x')R_\gamma(x')ds \tag{3}$$

where $\xi=(\xi_1,\xi_2)$, $x'=(x',y')$ are field point and source point respectively. $U_{\beta\gamma}$ and $H_{\alpha\beta\gamma}$ are the fundamental displacement and stress solutions* for a point load in the γ direction in an infinite medium. As ξ approaches a boundary point from inside the region, equation (2) reduces to an integral equation of the second kind for which the integral is defined in a Cauchy principal value (CPV) sense. For equation (3) the corresponding boundary integral is of the first kind and need not be considered as a CPV. For simplicity, a general boundary integral equation covering several cases can be written as:

$$p_\beta(s) = a \, \delta_{\beta\gamma} R_\gamma(s) + \int_{\partial D} G_{\beta\gamma} (s,s') R_\gamma(s')ds' \tag{4}$$

$$\beta,\gamma = 1,2$$

---

*These fundamental solutions are given in detail in Appendix A.

13
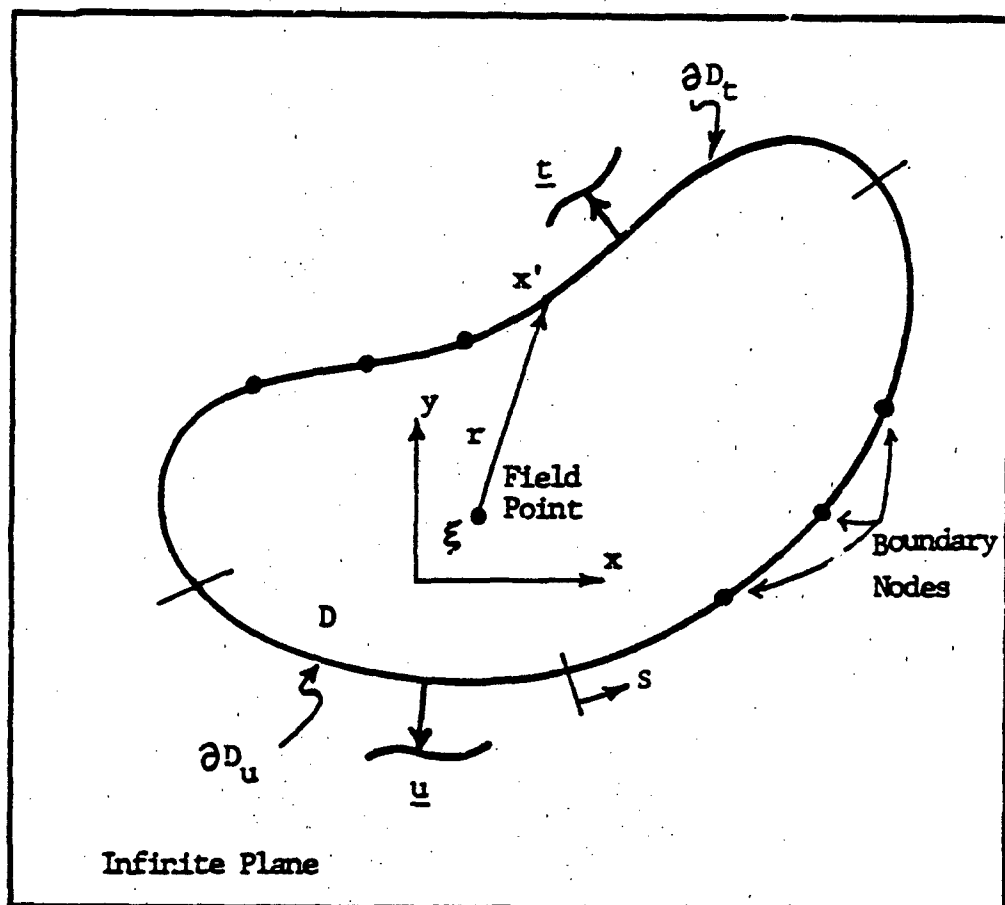
FIGURE 2-1. Geometry for the Boundary Element Method.

we consider three cases:

(i)   The pure displacement problem

$$a = 0$$

$$p_\beta = u_\beta$$

$$G_{\beta\gamma} = U_{\beta\gamma}$$

(ii)   The pure traction problem

$$a = 1/2$$

$$p_\beta = t_\beta$$

$$G_{\beta\gamma} = H_{\alpha\beta\gamma} n_\alpha$$

(iii)   The mixed problem (i.e., displacements are prescribed on ∂D_u and tractions are prescribed on ∂D_t) requires an appropriate combination of case (i) and case (ii).

In the numerical solution of equation (4) one can replace ∂D by N straight line segments ∂D_j, $j = 1, \ldots, N$ on which the point loads $R_\gamma(s_j)$ are approximated by piecewise constant functions $R_\gamma(s_j)$, $\gamma = 1,2$, $j = 1, \ldots$ N. If the boundary conditions are satisfied at the center of each segment then equation (4) reduces to a system of 2N simulataneous linear algebraic equations denoted by:

$$\underset{\sim}{A}\ \underline{R} = \underline{b}, \tag{5}$$

where A is a 2Nx2N coefficient matrix, $\underline{R}=(R_1, R_2, \ldots R_{2N})^T$ are the unknown point loads and $\underline{b}=(b_1, b_2 \ldots b_{2N})^T$ are the prescribed boundary conditions. The essence of the computation is the construction of A. From the discretized version of equation (4) it can be seen that A is N blocks of 2x2 matrices having elements:

$$(a_{\beta\gamma})_{ij} = \begin{cases} 1/2\delta_{\beta\gamma} & i = j \\ \int_{\partial D_j} H_{\alpha\beta\gamma}(s_i, s')n_\alpha ds' & i \ne j \end{cases} \tag{6}$$

$$(a_{\beta\gamma})_{ij} = \begin{cases} (a^*_{\beta\gamma})_{jj} & i = j \\ \int_{\partial D_j} U_{\beta\gamma}(s_i, s')ds' & i \ne j \end{cases} \tag{7}$$

where $(a^*_{\beta\gamma})$, $\beta,\gamma = 1,2$ have been computed analytically using Figure 2-2

15
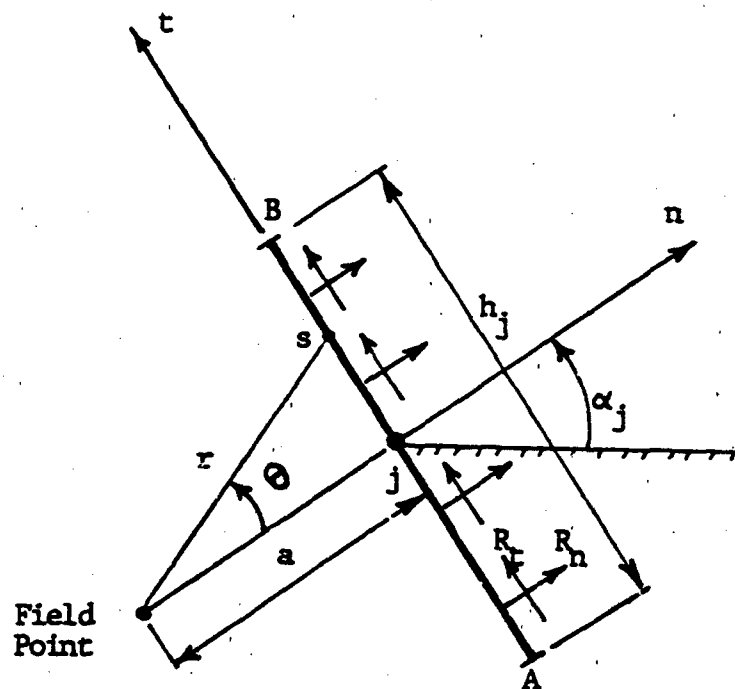
FIGURE 2-2. Geometry for Computation of $a^*_{\beta\gamma}$'s

$$(a^*_{\beta\gamma})_{jj} = \underset{a \longrightarrow 0}{\text{Limit}} \int_{-h_j/2}^{h_j/2} U_{\beta\gamma} \, ds$$

for both isotropic and orthotropic materials. In Figure 2-2, h_j is the mesh length. As $a \to 0$, the field point approaches the boundary point and the integrals over this mesh length become singular. The integrals are evaluated by first assuming that the unknown traction components R_t, R_n are constant over the mesh length. R_t, R_n can then be taken outside the integrals, and the resulting integrals can then be evaluated analytically for $a \neq 0$. The resulting values of $(a^*_{\beta\gamma})_{jj}$ are obtained by taking the limit as $a \to 0$. The results are:

(i) For the isotropic case

$$(a^*_{11})_{jj} = 2Q\, h_j(\ln(h_j/2)-1) + h_j\cos^2\alpha_j$$

$$(a^*_{12})_{jj} = (a^*_{21})_{jj} = h_j\sin\alpha_j\cos\alpha_j$$

$$(a^*_{22})_{jj} = 2Q h_j(\ln(h_j/2)-1) + h_j\sin^2\alpha_j$$

with $Q = (3-\nu)/2(1+\nu)$, where ν is the Poisson's ratio for material.

(ii) For the orthotropic case

$$(a^*_{11})_{jj} = -[(c_1A_1-c_3A_2)\cos^2\alpha_j + (c_4A_1-c_2A_2)\sin^2\alpha_j]h_j(\ln(h_j/2)-1)/2$$

$$(a^*_{12})_{jj} = -((c_1A_1+c_2A_2-c_3A_2-c_4A_1)\cos\alpha_j\sin\alpha_j)h_j(\ln(h_j/2)-1)/2$$

$$(a^*_{21})_{jj} = (a^*_{12})_{jj}$$

$$(a^*_{22})_{jj} = -[(c_1A_1-c_3A_2)\sin^2\alpha_j + (c_4 A_1-c_2A_2)\sin^2\alpha_j]h_j(\ln(h_j/2)-1)/2$$

where c's and A's have been defined in Appendix A.

The integrals in equations (6) and (7) have been computed numerically using a four-point Harris-Evans quadrature formula (3). This quadrature is useful when the integral is singular. In this formulation (the singular case), $i=j$ has been excluded, but in the adjacent segments (near singularities) this quadrature is helpful.

Once the system (5) is solved for $\underline{R}$, stresses and displacements at any internal field point can be computed from the discretized form of equations (2) and (3). The boundary element method is unable to predict stresses and displacements at boundary points. However, by excluding singular points (i.e., evaluating elastic fields analytically) and employing the Harris-Evans quadrature for the rest of the points, we can predict boundary fields (especially the stress concentration factors in the example problems) quite accurately.

The corresponding computer program, BEM (see Appendix B), is based on the formulation explained here and is written in FORTRAN 77.

17

2.3. Example Problems

A number of example problems were solved using the BEM program. All problems have a common geometry, namely, the lower section of the simple lap mechanical joint (see Figure 2-3.). Making use of the symmetry of the specimen (for the principal material and coordinate axis coincident), the final geometry analyzed is shown in Figure 2-4. Figure 2-5. is a schematic of the boundary element subdivision used. Both isotropic and orthotropic problems were solved; however, only orthotropic results are presented. All orthotropic problems were based on a particular glass-epoxy composite having the following compliances:

$$c_{11} = 5.00 \times 10^{-8} \ 1/psi$$

$$c_{12} = -1.05 \times 10^{-8} \ 1/psi \tag{8}$$

$$c_{22} = 4.76 \times 10^{-7} \ 1/psi$$

$$c_{33} = 1.18 \times 10^{-6} \ 1/psi$$

These compliances were measured for the laminate used in the experimental strain analysis phase of this project (see Section 3-8.).

Two items were investigated in this limited numerical study. The first involved hole size, i.e., the d/w ratio, and the second was the effect of various boundary conditions. Tables 2-1. through 2-4. shown with the enclosed figures are self explanatory and give selected solutions for these parameters. Full field stresses were computed but only ligament line (the line from the edge of hole to the edge of the specimen) stresses are presented. These stresses are particularly useful for two reasons: the maximum stress concentration is along this line (at the hole edge) and the appropriate summation of these stresses (forces) is a check on overall equilibrium. All computations were done on a Cyber 750 computer. Note that in the following subsection in which BEM is compared to FEM, both programs were run on the Prime 250 system. This system had graphics capability which permitted graphic display of computed data.

2.4. Comparison of BEM and FEM

As discussed earlier, one of the main objectives of this work is to make a comparison of BEM and FEM numerical procedures. For this purpose it was useful to run both programs on the same computer. The FEM computer code was available on the Prime 250 system. For this reason, the BEM code was adapted to the Prime 250 computer system. For this contract FEM-BEM comparison has been done only for the case of isotropic material with the simple joint in tension. This is the isotropic version of the results in Table 2-1. The comparison was based on a common boundary subdivision, i.e., in the BEM code 57 boundary elements corresponded to 134 quadratic FEM elements, see Figure 2-6. For this case, the stress concentration also is "known" (4). Results are summarized in Figure 2-6. and below:

18
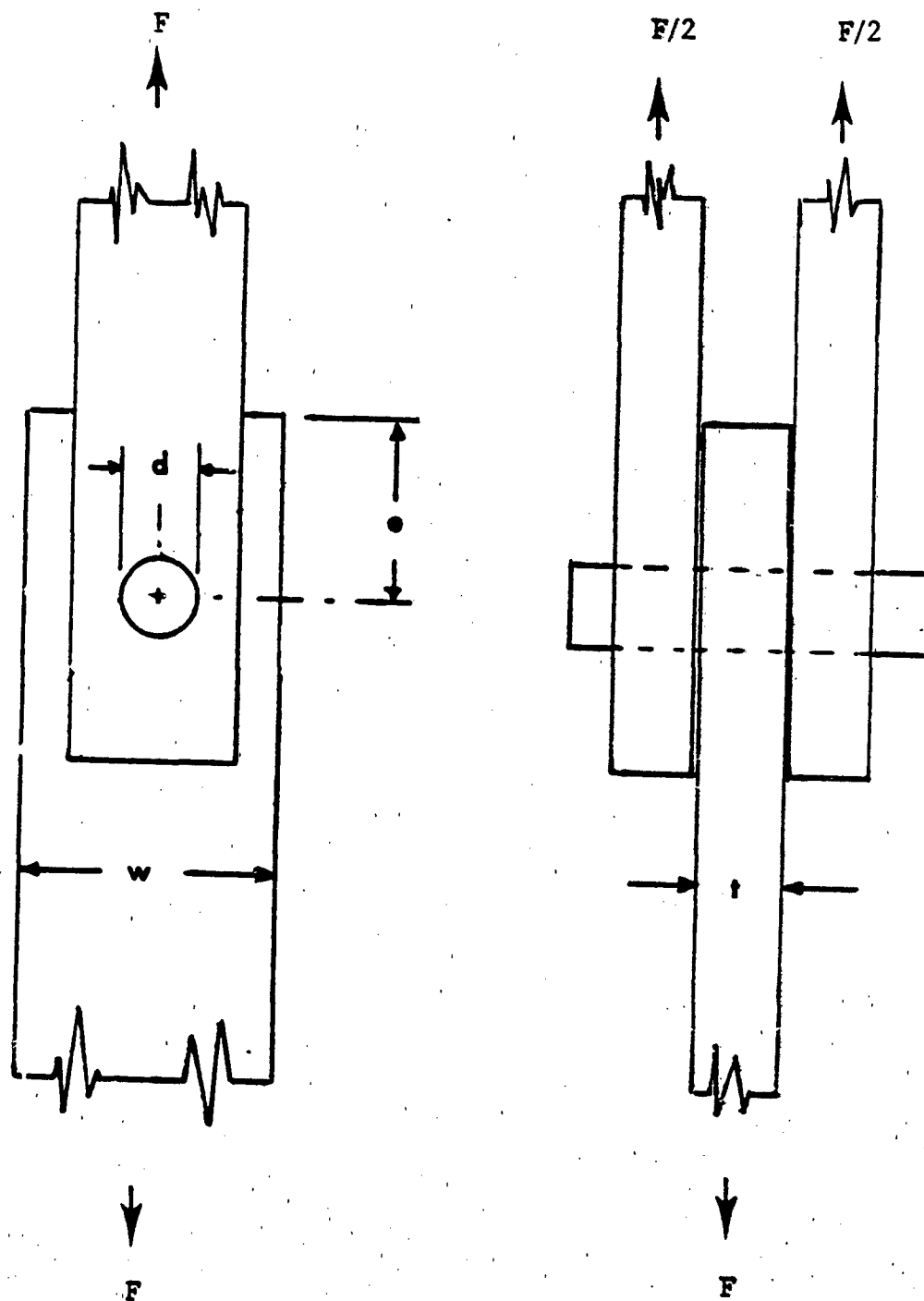
FIGURE 2-3. Double-lap Mechanical Joint.
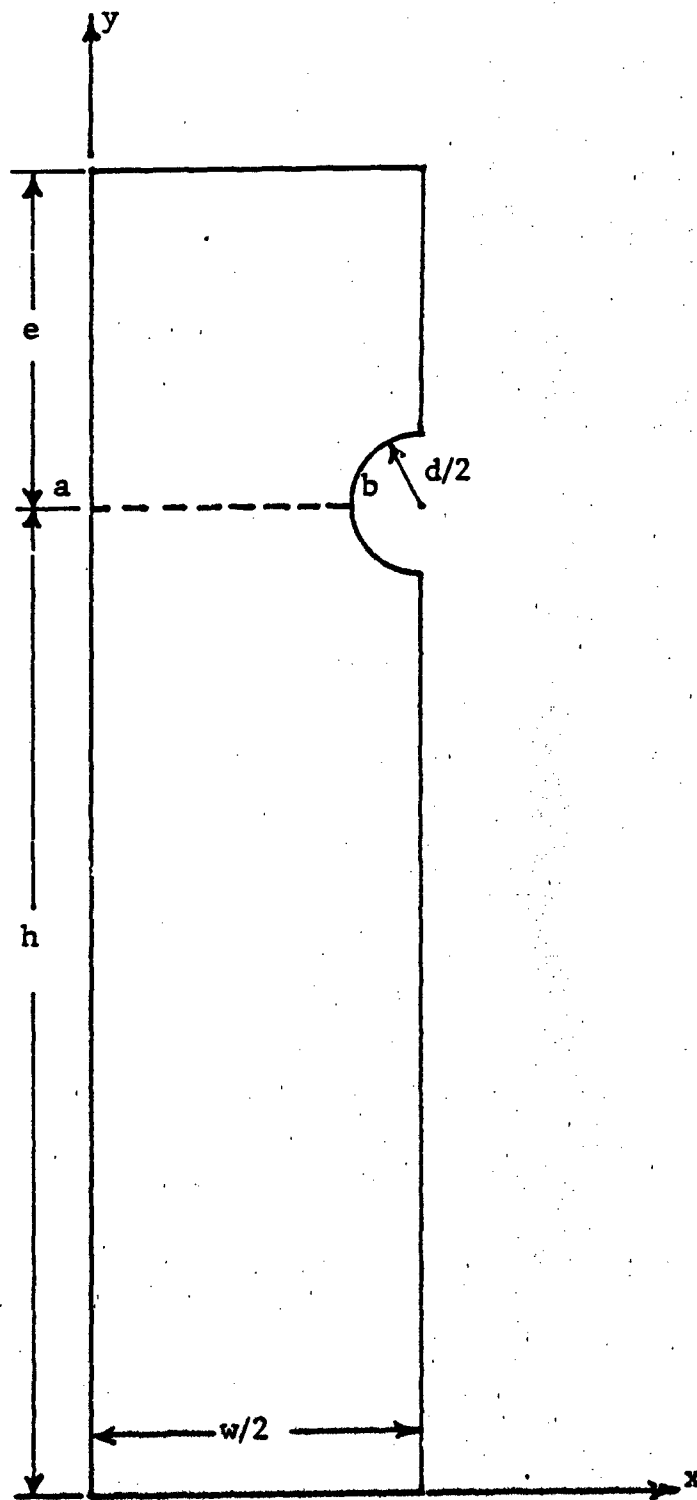
FIGURE 2-4. Geometry for the Example Problem
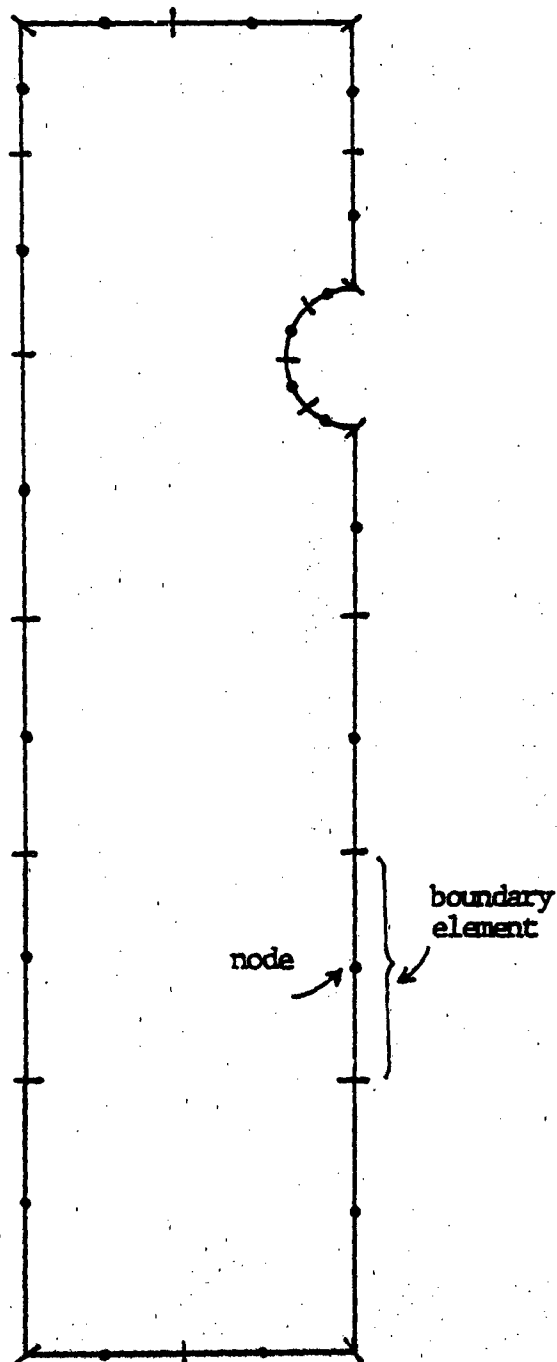
FIGURE 2-5. Schematic of Boundary Element Subdivisions.

TABLE 2-1.

Stresses along the ligament line ab
for an orthotropic composite.
Uniaxial Tension, d/w = .5,
N = 60 (boundary subdivisions)
d = 0.5
e = 0.5
h = 1.5
w = 1.0
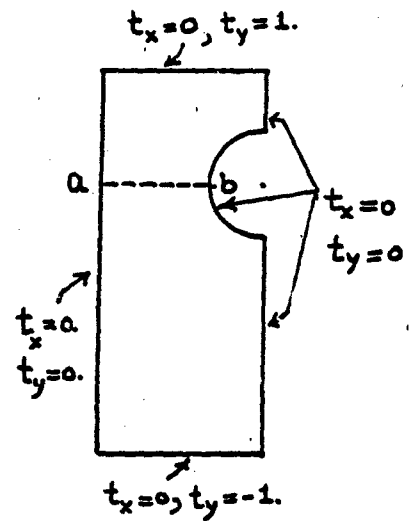
x	y	σ_{xx}	τ_{xy}	σ_{yy}
.02	1.5	.0070	.0015	-.1135
.04	1.5	.1593	.0091	.2379
.06	1.5	.2279	.0145	.5569
.08	1.5	.2861	.0189	.8721
.1	1.5	.3509	.0225	1.1847
.12	1.5	.4174	.0251	1.5085
.14	1.5	.4794	.0269	1.8589
.16	1.5	.5289	.0275	2.0496
.18	1.5	.5543	.0270	2.7191
.2	1.5	.5391	.0243	3.2888
.21	1.5	.5095	.0299	3.6290
.22	1.5	.4616	.0186	4.0195
.23	1.5	.3990	.0139	4.4765
.24	1.5	.3812	.0072	5.03.5
.25	1.5	-1.4308	.0082	6.4621

TABLE 2-2.

Stresses along the ligament line ab
for an orthotropic composite.
Cosine distribution of tractions on
the upper half of the hole, d/w = .5,
N = 60 (boundary subdivisions)

d = 0.5

e = 0.5

h = 1.5

w = 1.0
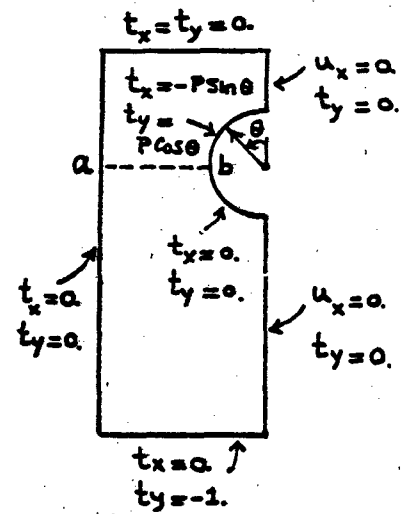
x	y	σ_{xx}	τ_{xy}	σ_{yy}
.02	1.5	.2160	-.1639	.7849
.04	1.5	.1100	-.1734	.9807
.06	1.5	.1555	-.1826	1.1347
.08	1.5	.2200	-.1826	1.2813
.1	1.5	.2775	-.1799	1.4318
.12	1.5	.3224	-.1643	1.5958
.14	1.5	.3531	-.1495	1.7830
.16	1.5	.3669	-.1323	2.0057
.18	1.5	.3575	-.1137	2.2820
.2	1.5	.3088	-.0949	2.6403
.21	1.5	.2595	-.8586	2.8645
.22	1.5	.1848	-.0770	3.1305
.23	1.5	.0826	-.0678	3.4528
.24	1.5	-.0037	-.0583	3.8640
.25	1.5	-.9524	-.2265	5.7545

TABLE 2-3.

Stresses along the ligament line ab
for an orthotropic composite.
Cosine distribution of tractions on
the upper half of the hole, d/w = .2,
N = 60 (boundary subdivisions)

d = 0.2

e = 0.5

h = 1.5

w = 1.0
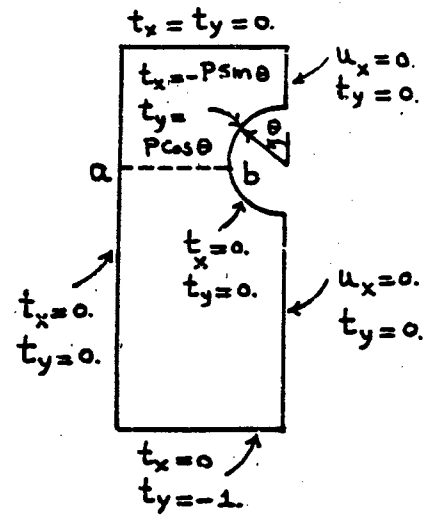
x	y	σ_{xx}	τ_{xy}	σ_{yy}
.032	1.5	.0494	.0626	.5133
.064	1.5	:0343	.0343	.5494
.096	1.5	.0415	.0189	.5899
.128	1.5	:0553	.0227	.6100
.160	1.5	.0727	.0332	.6496
.192	1.5	.0934	.0460	.6787
.224	1.5	:1198	.0616	.7285
.256	1.5	.1554	.0766	.7978
.288	1.5	.2066	.0909	.9295
.320	1.5	.2816	.1045	1.0894
.336	1.5	.3284	.1116	1.2948
.352	1.5	.3752	.1190	1.4420
.368	1.5	.4006	.1250	1.9735
.384	1.5	.3269	.1103	2.4196
.400	1.5	-.4279	.2449	3.3944

TABLE 2-4.

Stresses along the ligament line ab
for an orthotropic composite.
Fixed pin case,   d/w = .5,
N = 60 (boundary subdivisions)
d = 0.5
e - 0.5
h = 1.5
w = 1.0
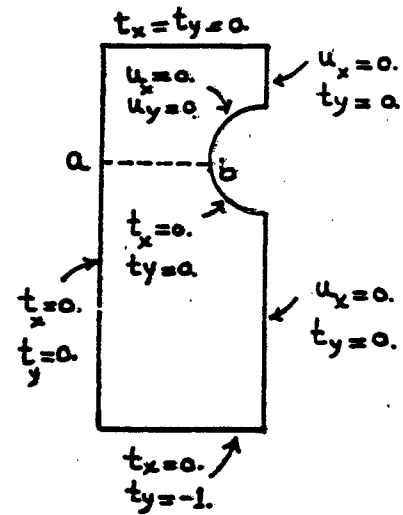

x	y	σ_{xx}	τ_{xy}	σ_{yy}
.02	1.5	.0019	-.0077	.8061
.04	1.5	.0232	-.0728	.8580
.06	1.5	.0324	-.1015	.9069
.08	1.5	.0390	-.1029	.9600
.1	1.5	.0442	-.1022	1.0203
.12	1.5	.0464	-.1007	1.0930
.14	1.5	.0432	-.0972	1.1815
.16	1.5	.0310	-.0913	1.3077
.18	1.5	.0040	-.758	1.4794
.2	1.5	-.0501	-.0467	1.7377
.21	1.5	-.0946	-.0221	1.9236
.22	1.5	-.1584	-.0116	2.1754
.23	1.5	-.2480	-.0527	2.5430
.24	1.5	-.3886	-.1264	3.2133
.25	1.5	-1.9566	-.9854	9.7269

1. FINITE ELEMENT (ANSYS)

(d = .2, e = 0.5, h = 1.5, w = 1.0)
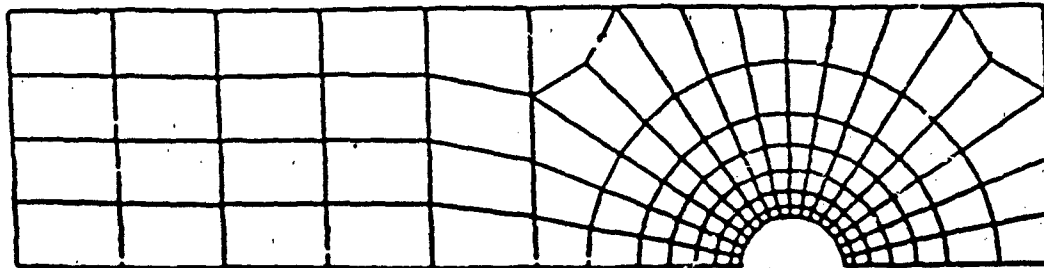
N = 134 Quadratic Elements

Results: For d/w = .2 K_I = 3.1102

Total CPU time: 177 sec.

2. BOUNDARY ELEMENT (BEM)

(d = .2, e = 0.5, h = 1.5, w = 1.0)
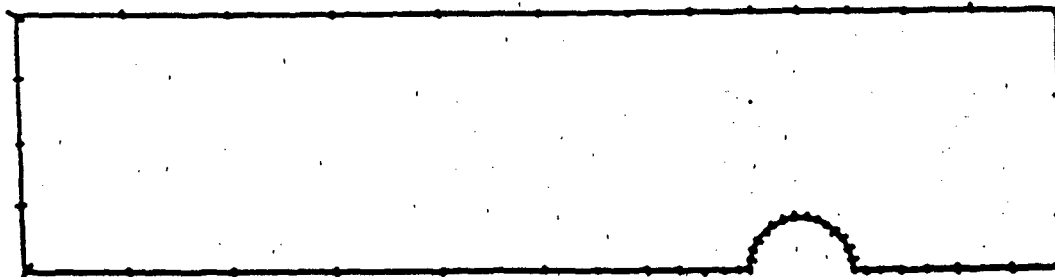
N = 57 Constant Elements

Results: For d/w = .2 K_I = 3. 0951

Total CPU time: 27 sec.

FIGURE 2-6. FEM and BEM Subdivision Schemes for the Mechanical Joint
Problem.

FEM	EXACT	BEM
$K_I = 3.1102$	$K_I = 3.1352$	$K_I = 3.0951$
CPU time = 177 sec.		CPU time = 27 sec.

Note that BEM represents a significant reduction in computer time over FEM. This savings depends to some extent on the particular case, how many field points are required, and so on.

3.0. EXPERIMENTAL METHODS AND RESULTS

3.1. Introduction

The experimental components of this investigation encompassed two phases. Techniques appropriate to the problem and the material were developed. Some studies of composite pin-loaded specimens were carried out. In actuality, both phases ran simultaneously, so the program was rather complex and open-ended.

The primary experimental method uses Moire interference with Fourier optical processing of grid photographs.* Rugged grids are applied to the specimen by vacuum-deposition, and these grids are recorded using high-resolution techniques for each state of the specimen. Sequential recording of grating replicas and subsequent coherent optical processing to obtain enhanced fringe patterns, often with multiplied sensitivity, allow quantitative comparisons between any two states of the specimen at any later time. Such a procedure is especially advantageous in nonreversible structural testing.

A publication (5) discussing the theoretical basis and showing an application of this Moire technique is duplicated in Appendix C. Complete descriptions appear in Air Force reports and papers by Cloud's group (6 to 12) so further description is not needed here.

It is worth noting that this version of the Moire method can be used in a "dirty" environment. It is tolerant of poor quality or course grids and poor photographic reproduction of the gratings. The approach has been used in difficult situations involving high temperatures (up to 1,500°F) long times (1,000 hours) and in the presence of convection currents, vibrations, and so on (6). The procedures appear to have great promise for application in field investigations of displacement and strain in structures of any material.

It soon became clear that the Moire technique as summarized above has a strain sensitivity which is marginal for work on composites, as was expected. Consequently, while this method was being used on the first

---

*In this report, grating means a set of parallel lines, while grid means a pair of orthogonal gratings -25 sets of lines at 90°.

27

specimens in this project, a program to extend the sensitivity by a factor of 10 or more was begun. Both endeavors were successful. In order to compare theoretical and experimental results in this project, the constitutive properties of the material studied had to be measured. This aspect of the experimental work was also successful.

This section describes first the specimen materials and preparation, including the creation of Moire grids. The essential details of the Moire process leading to plots of strain are then outlined. Results obtained in this way are given, and interesting aspects of these data are discussed. The experiments to determine material properties for the composite are described and the results given. Finally, the high-sensitivity techniques are described in brief, and some results which illustrate the promise and flexibility of the method are reported.

3.2 Specimen Fabrication and Material Specification

The material used for this investigation was fiberglass-epoxy laminate with woven fibers (R1500/1581, 13 plies, 0.14 in. thick) supplied by CIBA-GEIGY, Composite Materials Department, 10910 Talbert Avenue, Fountain Valley, California 92708.

The dimensions of the specimens are shown in Figure 3-1. It has been shown by Horgan (13) that, when working with composites, the end effects persist over distances of the order of several widths of the specimen. This stress channelling does not seem to be so severe in this case based on the results of the Moire patterns obtained, probably because of the reinforcing in the transverse direction. To be safe, however, the specimens were designed to be quite long and narrow.

The specimen was cut with the fiber oriented along the direction of the loading. Grating application techniques are described in section 3.3. Subsequent to applying the gratings, the fiducial marks, identifers, and code marks were applied with Presstype lettering. The specimen was then ready for recording a baseline Moire grating photograph, loading through the hole by means of a pin, and recording at-strain grating images.

3.3. Specimen Gratings

Application of the Moire effect to any problem depends on the successful deposition of line grids (or dots) on the specimen material.

The photoresist approach to creating grids on the specimens was chosen because it is fairly simple, requires minimal special equipment, and is well proven in the contractors' laboratory. Photoresists for Moire applications have been studied and described in detail by Luxmoore, Hollister and Hermann (14,15,16). Cloud and co-workers (6 to 12) have used this approach successfully.

The photoresist chosen was Shipley AZ1350J provided by the Shipley Co.,

FIDUCIAL MARKS

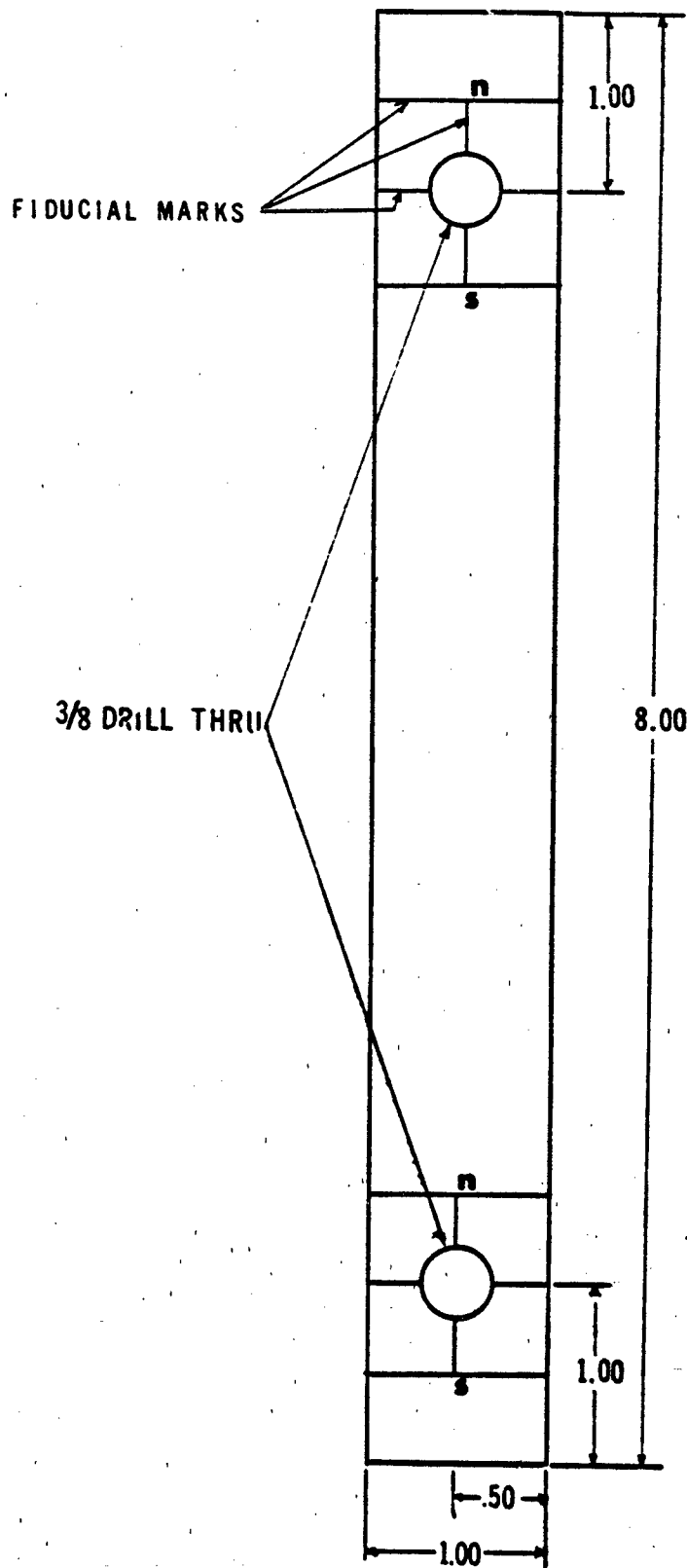3/8 DRILL THRU

1.00

8.00

n

s

n

s

1.00

.50

1.00

Figure 3-1.   Dimensions of the test coupon.

Newton, Mass. The companion thinner and developer were purchased with the resist.

It is desired for Moire work, as with most other photoresist usage, that the resist coating be thin and uniform. Common application methods include spinning, dipping, spraying, wiping and roller coating. The spinning and wiping techniques were found deficient in that they always left some build-up near the hole of the fastener boundary, that is, in the region of greatest interest.

Attention settled, therefore, upon the spraying method. An artist's airbrush was obtained and a spraying technique which gave satisfactory uniformity and coating thickness was worked out by trial and error. Superior results were obtained by thinning the resist. Testing was conducted to establish a balance of resist-thinner proportions, air pressure, airbrush nozzle opening, spraying distance, and brush motion.

In order to produce coatings of the desired thickness, the photoresist required thinning. The proportions arrived at through trial and error were by volume, one part AZ1350J to two parts AZ thinner. The air pressure provided by "canned air" sold in art supply stores was satisfactory for the Paasche type H-3 airbrush. The best nozzle setting for the airbrush used was 1-1/2 to 4 full turns open from the closed position. The spraying procedure which was developed called for laying the clean and dry specimen inclined at about 80° to the horizontal. The airbrush containing the resist was held about 12 in. from the specimen. Flow of the atomized resist was begun and allowed to stabilize for about one or two seconds, after which the spray was quickly shifted onto the specimen. At the range the air flowed, it was necessary to sweep the brush from left to right to cover the whole surface. Care was taken to assure that the spray fan did not overlap the previously applied wet coating, otherwise small bubbles of photoresist started to form, yielding a nonuniform surface. It was absolutely necessary to start the spray well before bringing it to bear on the specimen, as some coarse droplets are expelled at the beginning of flow.

Coating thickness was controlled by spraying time and number of strokes (or coatings). Best results were obtained with one single layer of resist.

If the coating did not appear satisfactory, it was removed using either thinner or acetone. This operation was performed as quickly as possible to avoid dissolving the surface of the specimen. The surface was then immediately washed with running water to get rid of any excess of acetone. After the specimen dried at room temperature, another coating of photoresist was applied. The coated specimens were placed inside a light-tight container to await exposure and development of the grating image.

30

3.4. Printing Grating onto Specimen

The Moire grid was printed on the photoresist coating on the specimen by a simple contact printing procedure in which a grid master was held in close contact with the specimen and the assembly exposed to ultraviolet light from a Mercury lamp. Figure 3-2. summarizes the process of applying the grids.

The master grid used to print the grid on the specimen was made by using a fine metal mesh with an orthogonal array of holes. In this study, Nickel mesh with 2,000 lines per in. was used. First, a Nickel mesh was held in close contact with a piece of flat glass by spreading soap solution over it and then removing the surplus with filter paper. Then the corners of the piece of mesh were fastened to the glass with adhesive tape.

The Mercury lamp which was used has a power of 200 Watts. The distance from the lamp to the master grating-specimen assembly was 20 in. The time of exposure was 30 seconds. The newly exposed photoresist was developed according to manufacturer's instructions in the standard Shipley AZ developer diluted with water.

Next the specimen with its photoresist grid was placed in a vacuum deposition unit (Denton D.V. 502 high vacuum evaporator) and a film of aluminum was deposited over the whole surface. The result is a relief grid in the metal coating with excellent reflectivity. Aluminum was chosen because of its ability to resist tarnishing, its high reflectivity in thin films, and its low cost.

3.5. Grid Photography

The complete state of strain throughout an extended field can be determined from Moire fringe photographs obtained through superposition of a submaster grating with deformed and undeformed (baseline) specimen grid replicas. Such superposition yields baseline Moire fringes and data (at strain) fringe patterns.

The set up used to accomplish the high resolution photography of the specimen grid is sketched in Figure 3-3. The camera used was a Horseman 4X5 bellows model. The lens was a Carl Zeiss S-planar with focal length of 120mm and a maximum aperture of 5.6. The system rested upon a granite optical table and the camera was set up to give a magnification factor of one. The specimen was placed in the loading frame (loaded under tension). The light sources were two flash lamps which were activated by an electronic triggering mechanism.

Focus of the specimen image was very critical in this high resolution situation. The ground glass of the camera was not satisfactory for this critical work because it was too coarse and because such focus plates are often not exactly in the photoemulsion plane. For focusing, a blank plate of the thickness and type used in the photography was developed and fixed and then mounted in a 4X5 plate holder which had the separator removed.

1)

SPR

SPECIMEN

HG
LAMP

2)

SUBMASTER
SPR

SPECIMEN

3)

SPR

SPECIMEN

4)

THIN FILM OF AL
SPR

SPECIMEN

SPR = Shipley Photo Resist
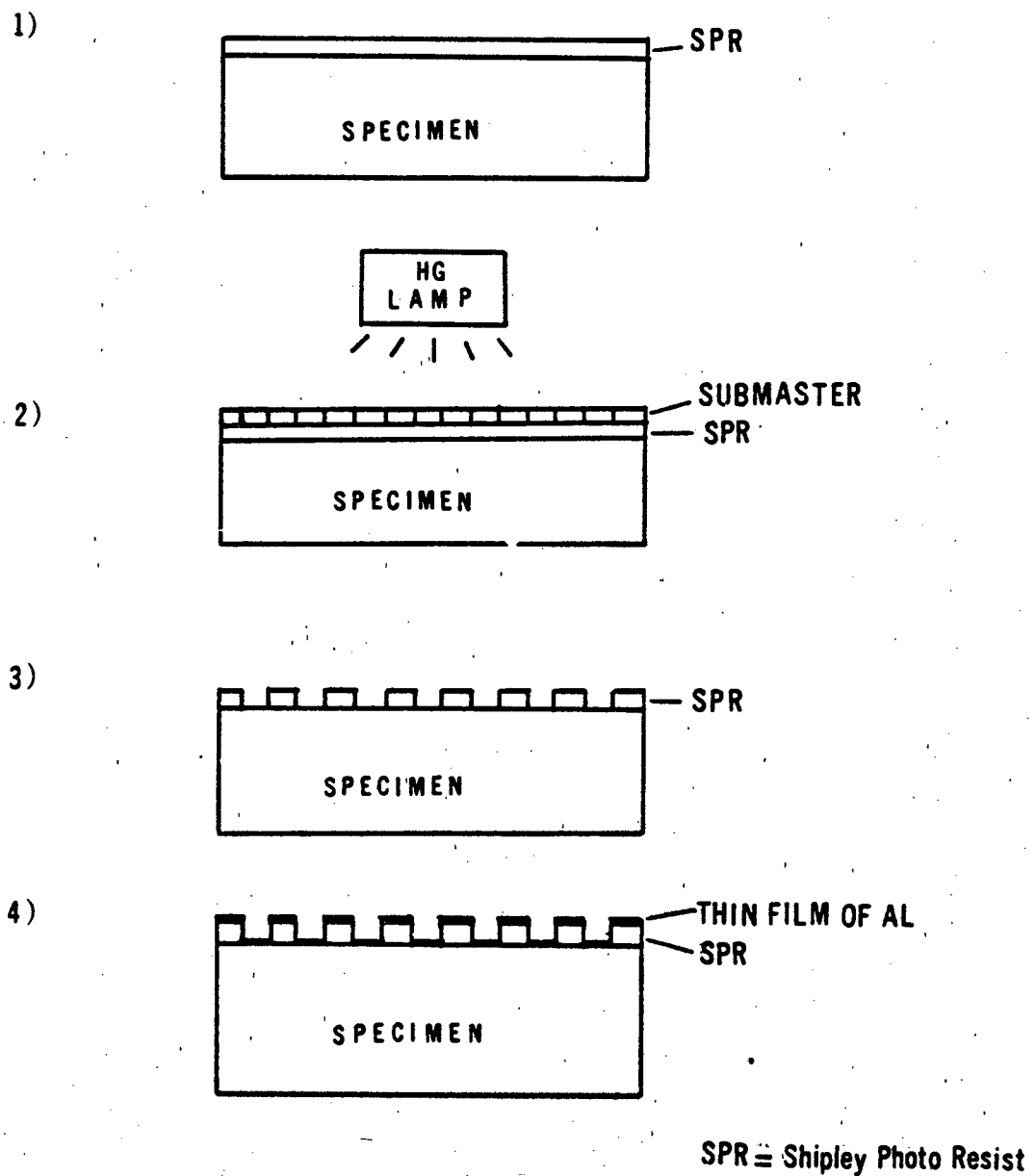
Figure 3-2.   Grating production process.

32

TOP VIEW

Strobes

45°

Specimen

4x5 View Camera

SIDE VIEW

Strobes

45°

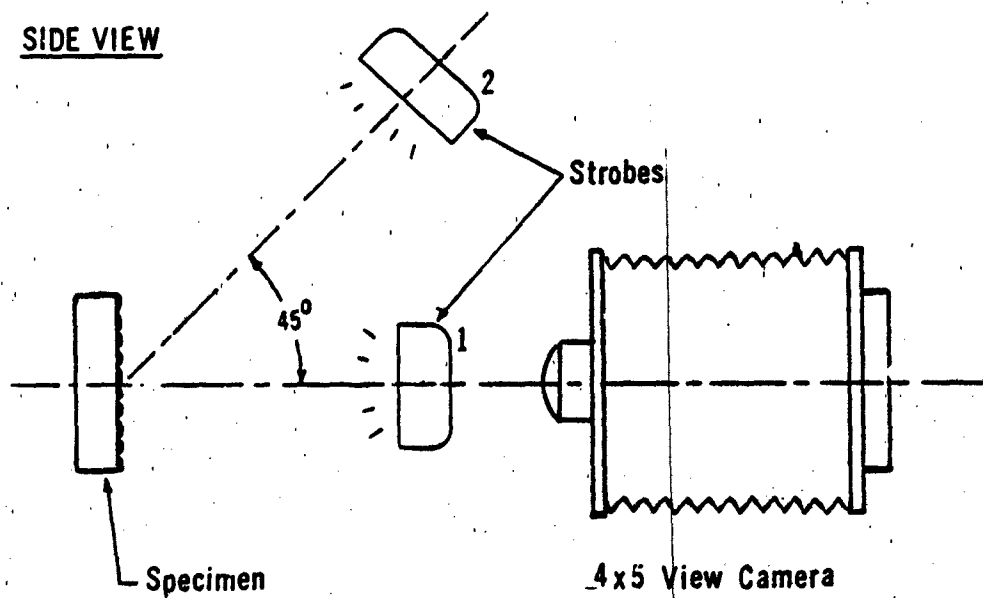Specimen

4x5 View Camera
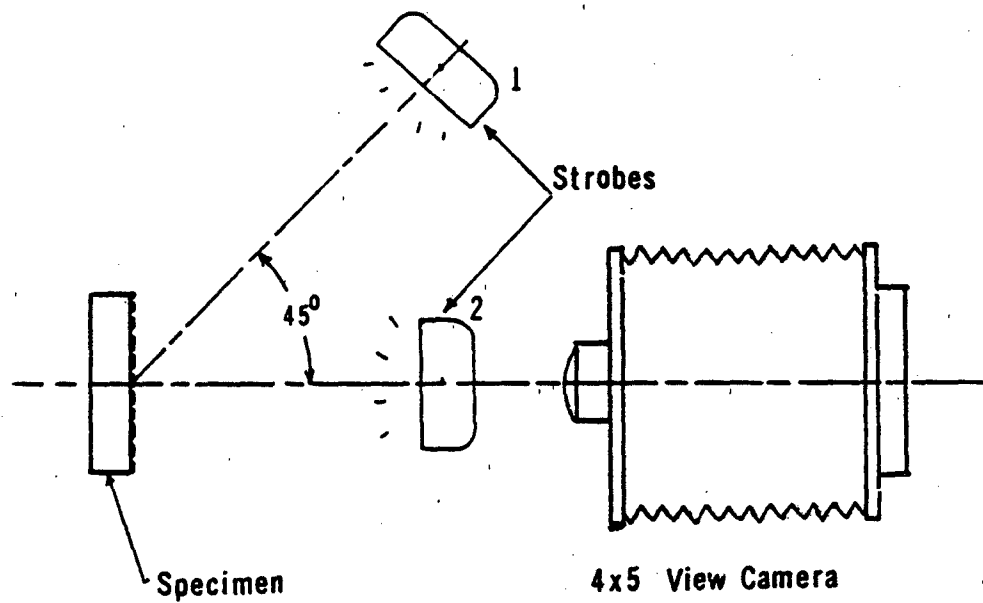
Figure 3-3. Set-up for grating photography.

33

The image of the specimen in the emulsion was examined with a 160X microscope which had been focused first on the image of the specimen surface. This process facilitated bringing emulsion and image into the same plane.

After checking that the image of the specimen was perfectly focused over its entire area and that the desired magnification was correct, the camera was locked in place to avoid losing the focus during the loading of the photo-plate.

The right exposure was determined by trial and error using Kodak high-speed holographic film (type SO-253, 4X5 in.). After getting the best grid-replica from Kodak film, the data and baseline grids were recorded by using Kodak high speed holographic plates (type 131-02, 4X5 in.). In order to get the right exposure, the maximum aperture was used to avoid losing sharpness of the grating, and the intensity of the flash lamps was reduced by adding ground glass pieces in front of the flashlamps. These glasses cut down the intensity of the light by roughly one f-stop per piece. Also, it is worth noting here that the angle of incidence of the illumination was chosen by trial and error to give the best contrast in the grating image. Shadows of the three-dimensional grid structure evidently play an important role in grating visibility. The exposed 131-02 plates were individually developed in Kodak HRP developer for three minutes and fixed in Kodak fixer for the same amount of time.

After completion, each grating plate was examined and inspected for diffraction efficiency to assure that the photography had been successful. It was labelled with specimen number, loading, and magnification conditions for future reference and stored in a rack to await optical construction of Moire fringe patterns.

3.6. Summary of Optical Processing to Create Fringe Patterns

The grating photographs of this experiment produced an assembly of photographic plates of the undeformed (baseline) and deformed (data) specimen gratings as well as a submaster grating having an integer multiple of the specimen's grating spatial frequency. The creation of Moire fringe patterns from these plates and the reduction of Moire fringe data have been described in detail (9 to 12). The steps required to produce Moire fringe photographs from these grid records were as follows:

1. A photoplate of the undeformed specimen grid was superimposed with a master grating having a spatial frequency of 1000 lpi (which was half the spatial frequency of the specimen grating) plus or minus a small frequency mismatch.

2. The superimposed gratings were clamped together and placed in a coherent optical processor and adjusted to produce a correct base line (zero strain) fringe pattern at the processor output, where it was photographed. This photograph corresponded to the superposition of the 2nd diffraction order of the master grating

34

with the first diffraction order of the corresponding specimen grating.

3. Steps 1 and 2 were repeated for the other component of the specimen grid i.e. the grating at 90° to the first one.

4. Steps 1 to 3 were repeated with the photographs of the deformed grid in order to create the "data" or "at strain" fringe patterns. The same submaster plate was used.

5. The fringe patterns were enlarged and printed with high contrast in a convenient size equivalent to about 5 times the actual specimen dimensions.

6. The prints were sorted and coded for identification.

7. Computer digitizing, data reduction, and plotting were performed on each photograph.

8. Digital processing of Moire data finished the analysis.

Digitization of the fringe patterns and subsequent data reduction followed the procedures described in detail by Cloud and colleagues (9 to 12). Some of the essentials are reproduced in Appendix C.

3.7 Experimental Results

In this investigation, the specimen had a two-way grating (a grid). By using the optical processor, a Moire fringe pattern was formed separately for each direction. One pattern was formed to get horizontal fringes (perpendicular to the direction of loading), and this fringe pattern was used to measure strain in the direction of loading. The other pattern was formed with vertical fringes (same as direction of loading); fringes in this direction were used to measure transverse strain (perpendicular to the direction of the load). The photograph of the fringe pattern was recorded separately for each direction and for each loading step. Sample photographs of the Moire fringe patterns obtained from the composite material fastener specimen for the horizontal and vertical directions are shown in Figures 3-4. to 3-7.

Figures 3-8. through 3-11. show the measured strain ϵ_x and ϵ_y for several different lines on the specimen. The whole-field nature of the Moire method means that a great deal of data are generated. Such data are always difficult to present and assimilate. The plots shown here are a reasonable compromise between completeness and confusion. The next step is to develop strain contour maps, which would be easier to understand at a glance. Such a step was not within the scope of this project. Programs for three dimensional computer graphics representations of the strain contours are being developed by the investigators.
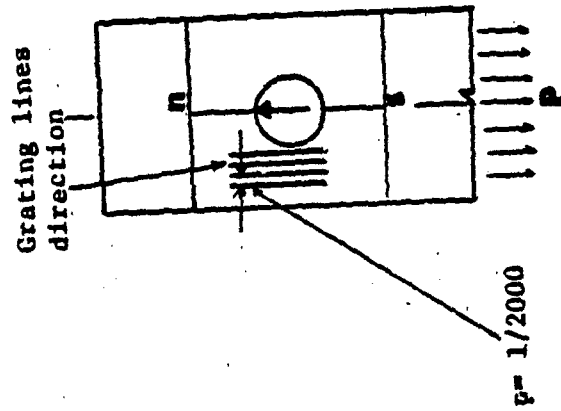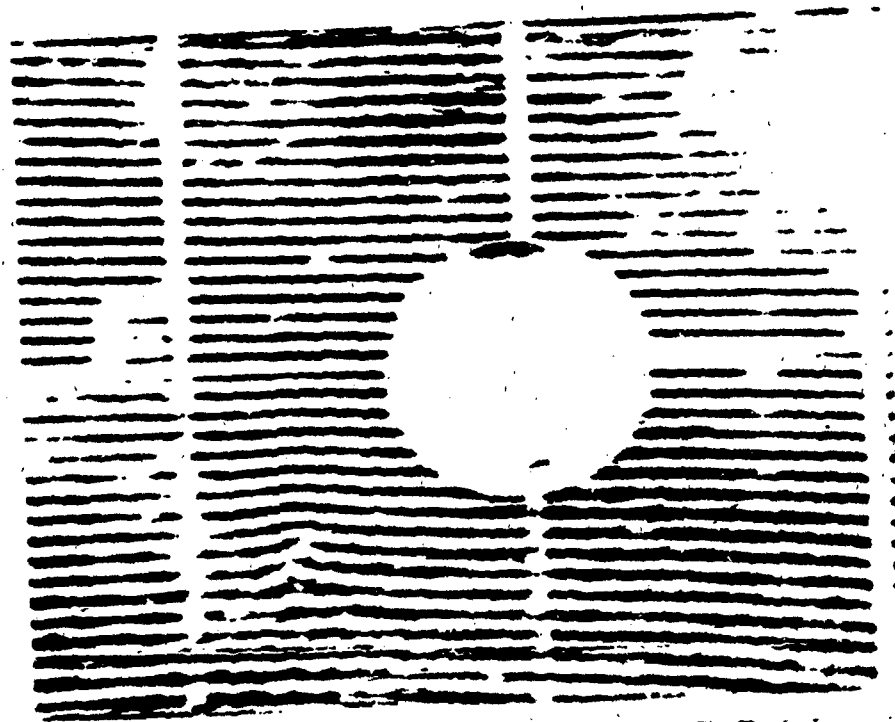
Figure 3-4. Photograph of Moire pattern showing displacements perpendicular to load line for zero load with pitch mismatch.
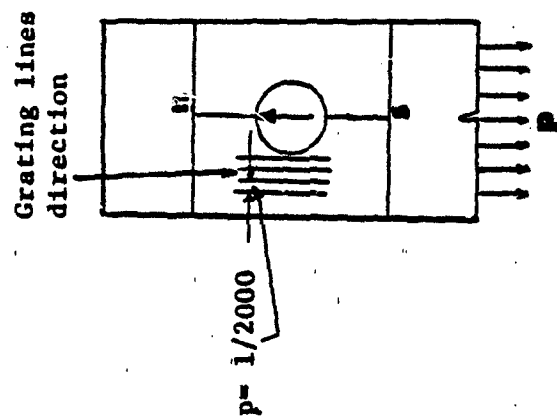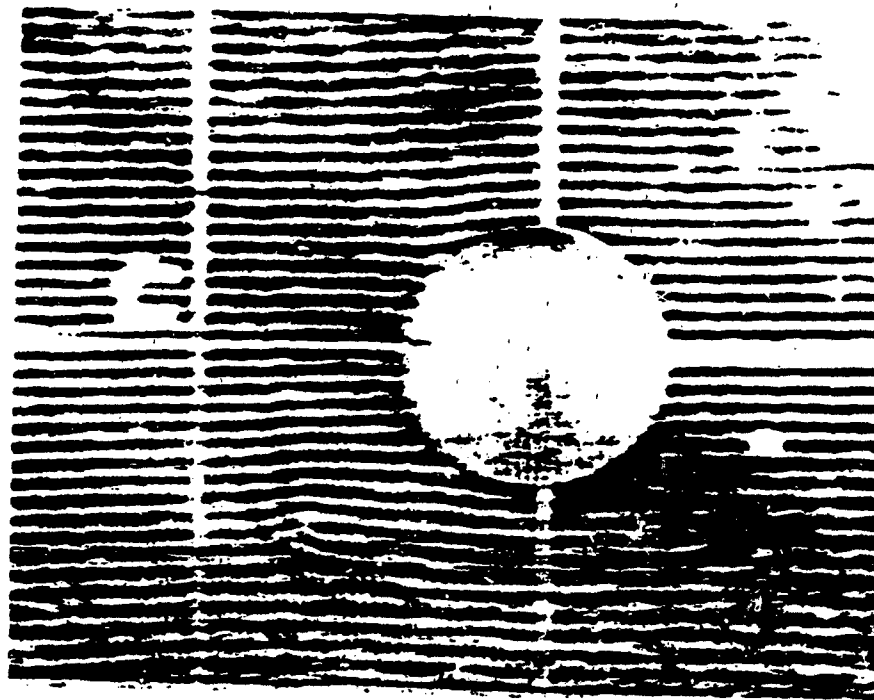
Figure 3-5. Photograph of Moire pattern showing displacements perpendicular to load line for 400 lbs. load with pitch mismatch

37
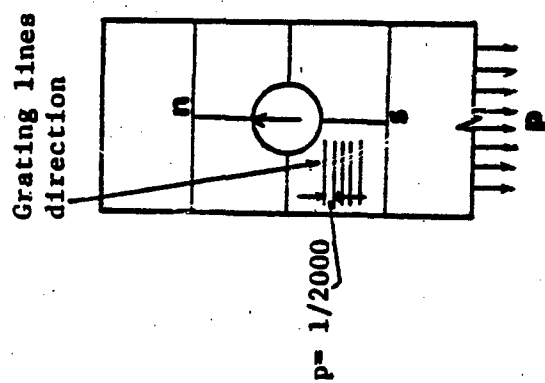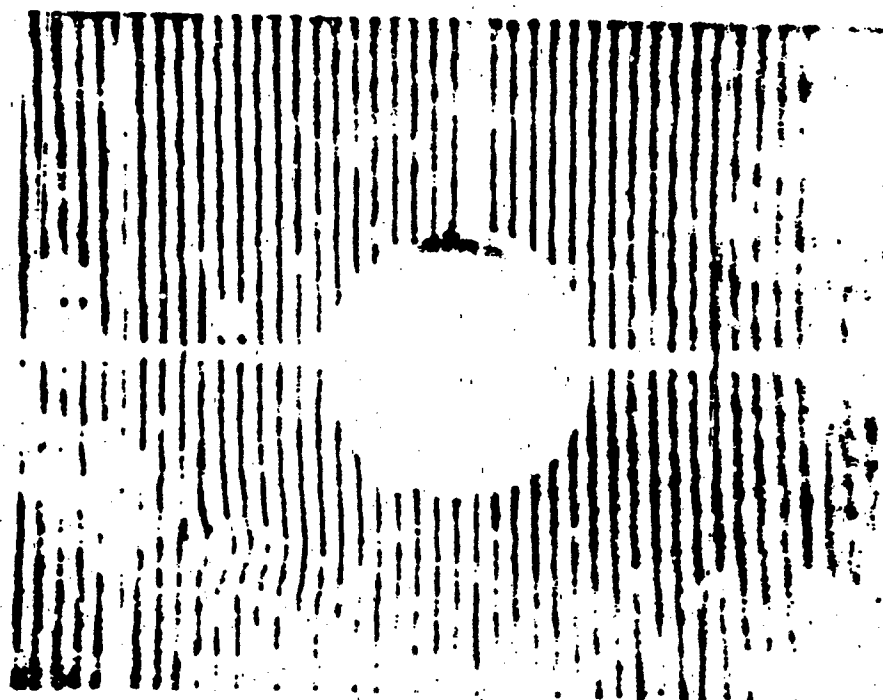
Figure 3-6. Photograph of Moiré pattern showing displacements parallel to load line for zero load with pitch mismatch.
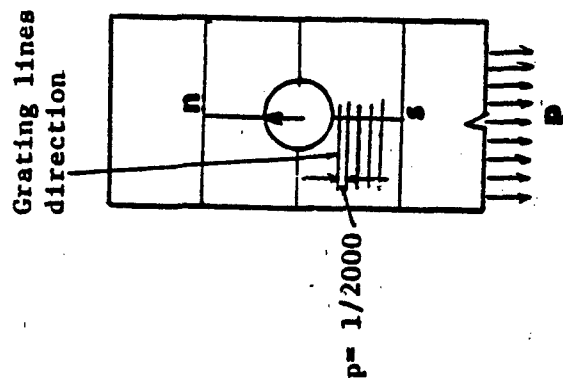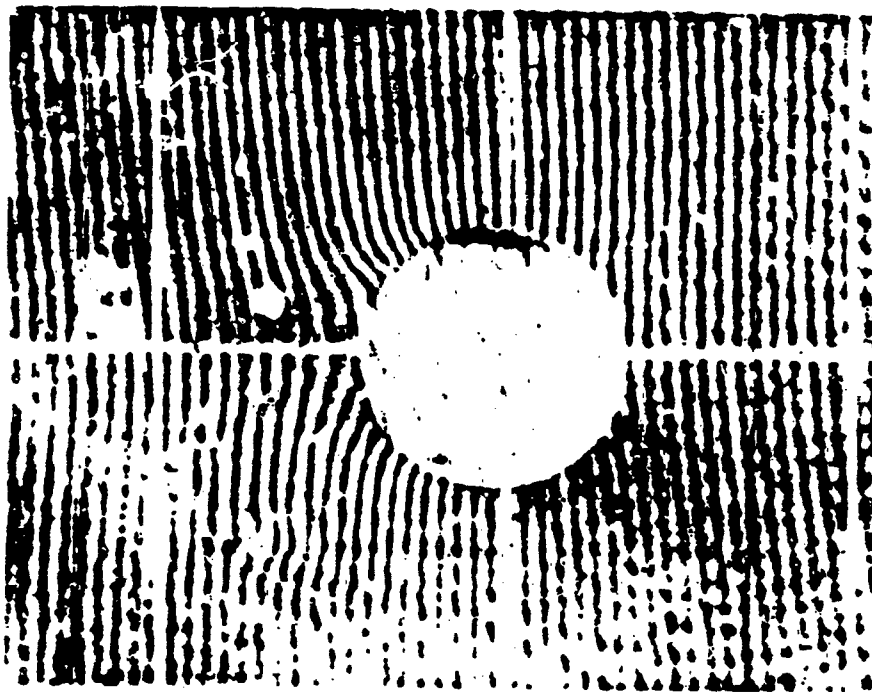
Figure 3-7. Photograph of Moire pattern showing displacements parallel to load line for 400 lb. load with pitch mismatch.
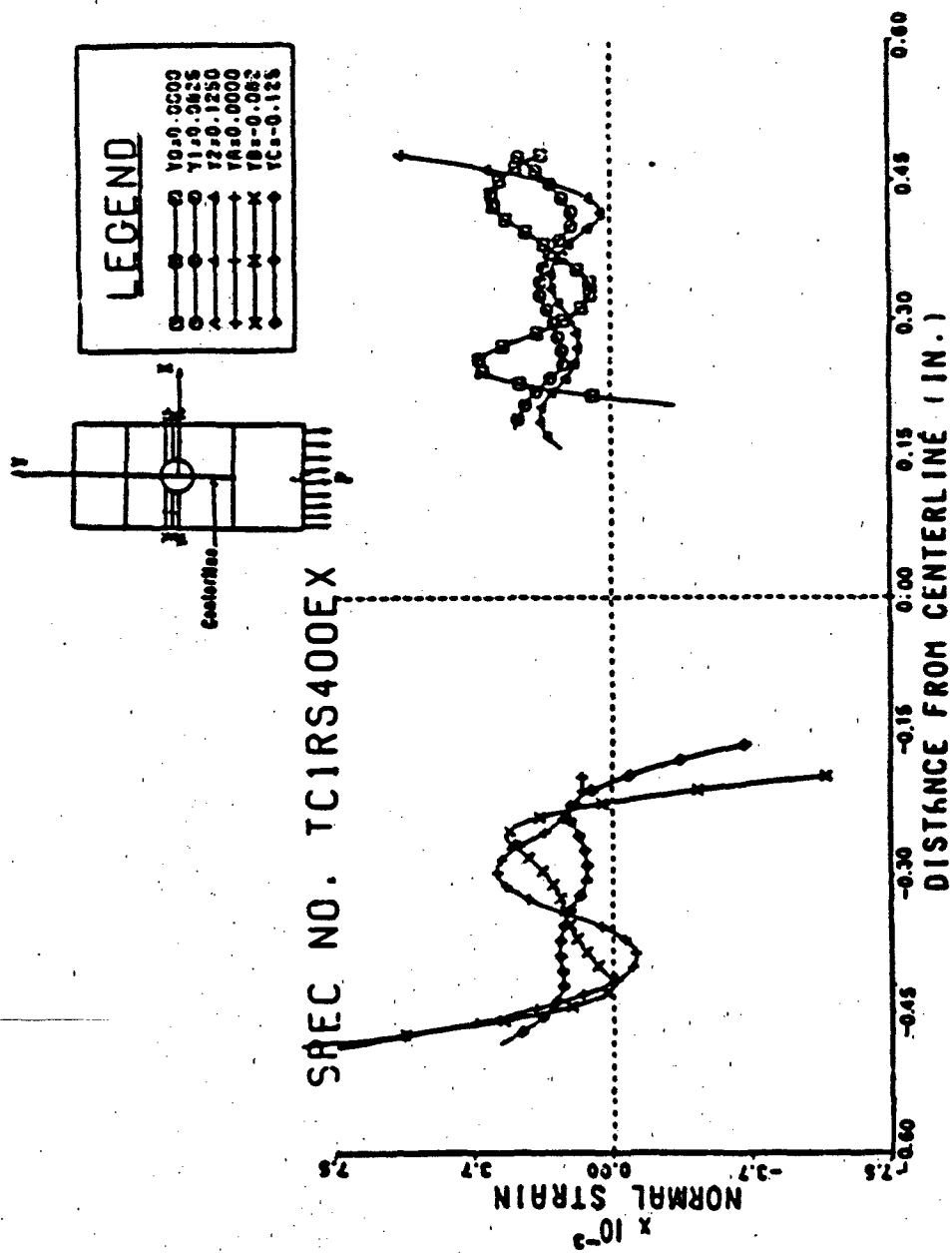
Figure 3-8. Strain perpendicular load to axis (ϵ_x) along several lines in the ligaments of fastener hole.

40
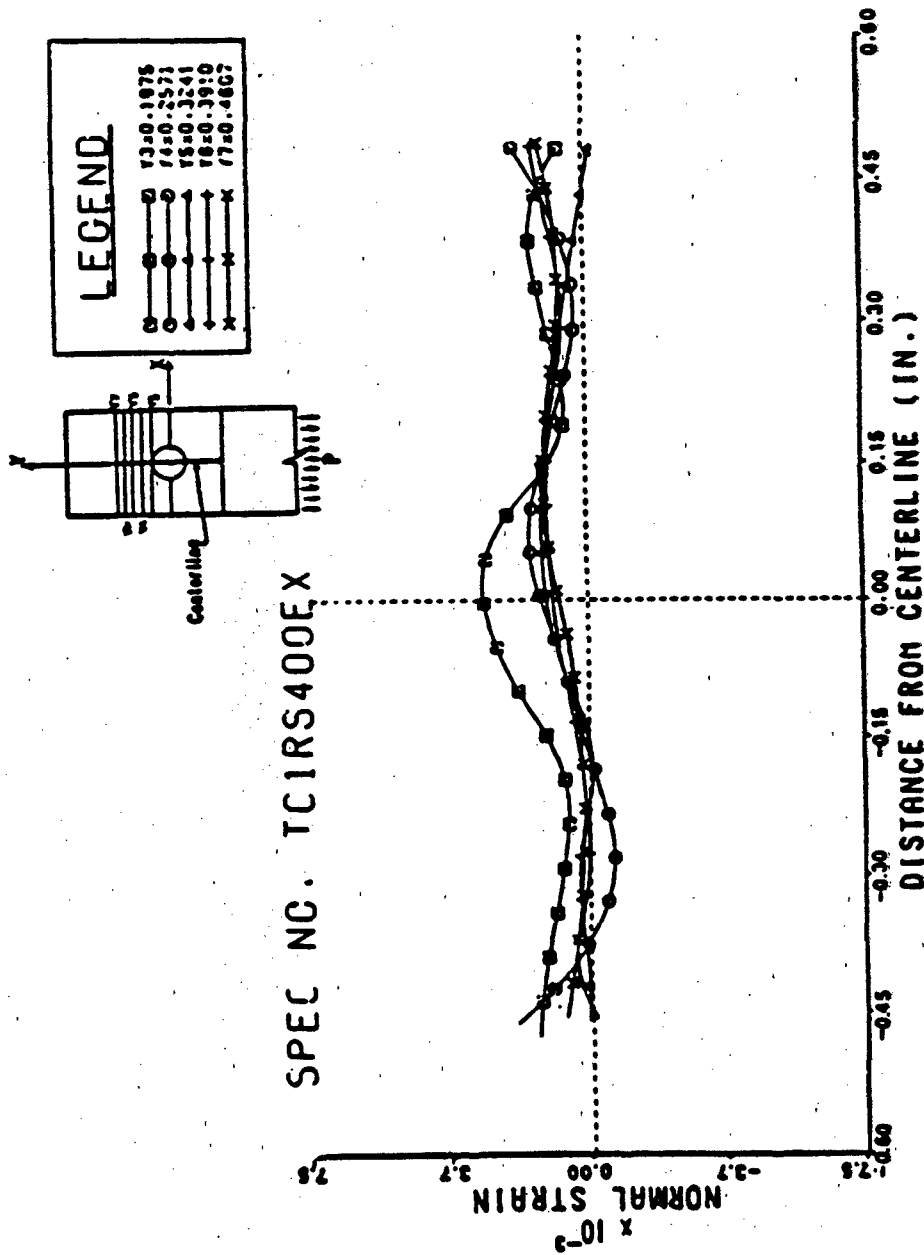
Figure 3-9. Strain perpendicular load to axis (ϵ_x) along several lines in bearing region near hole.

41

SPEC NO. TC1US400EY

LEGEND

X3=0.1975
X4=0.2521
X5=0.3241
X6=0.3910
X7=0.4607

DISTANCE FROM CENTERLINE (IN.)

NORMAL STRAIN
x 10⁻³
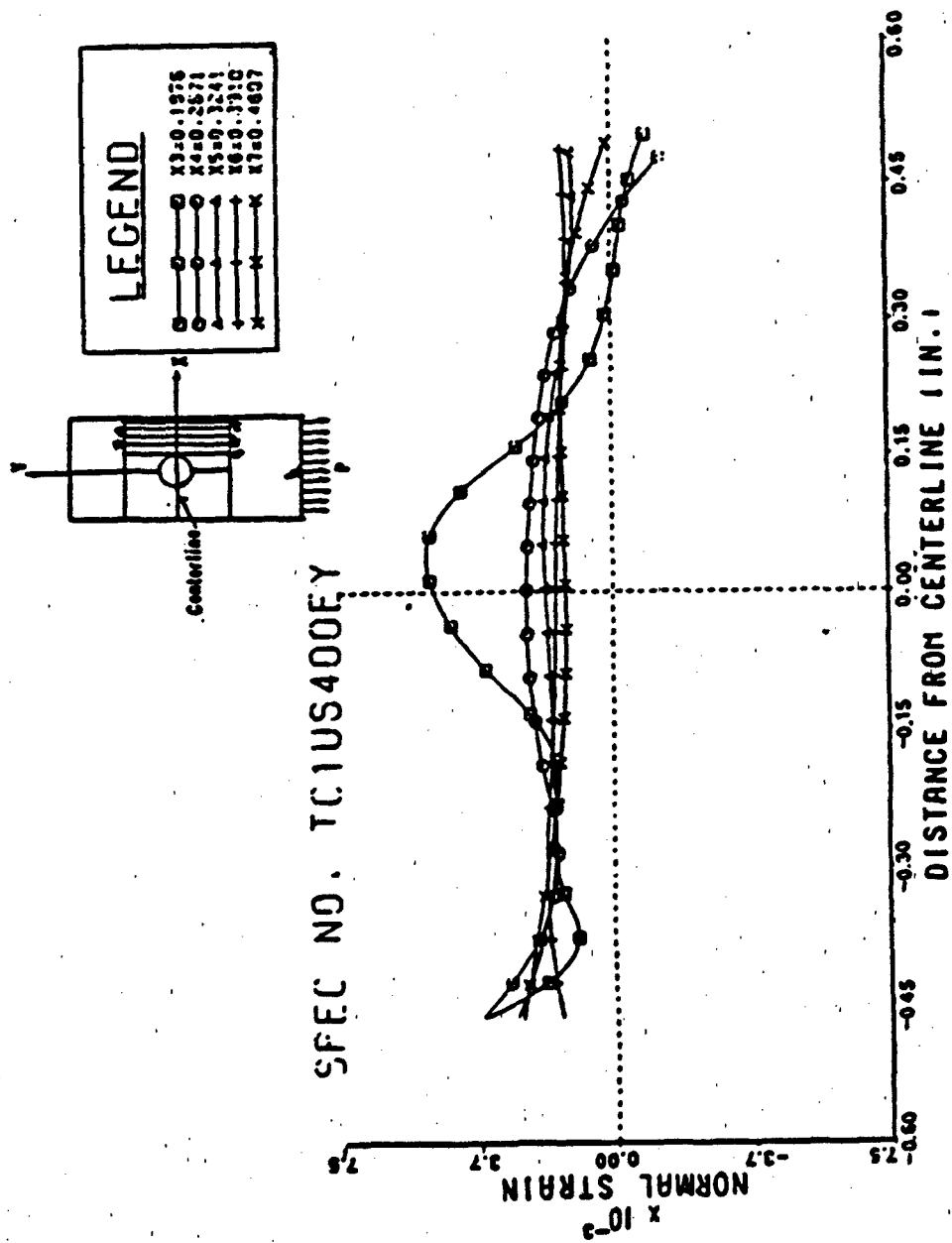
Figure 3-10. Strain parallel to load axis (ϵ_y) along several lines
encompassing a ligament region.

42
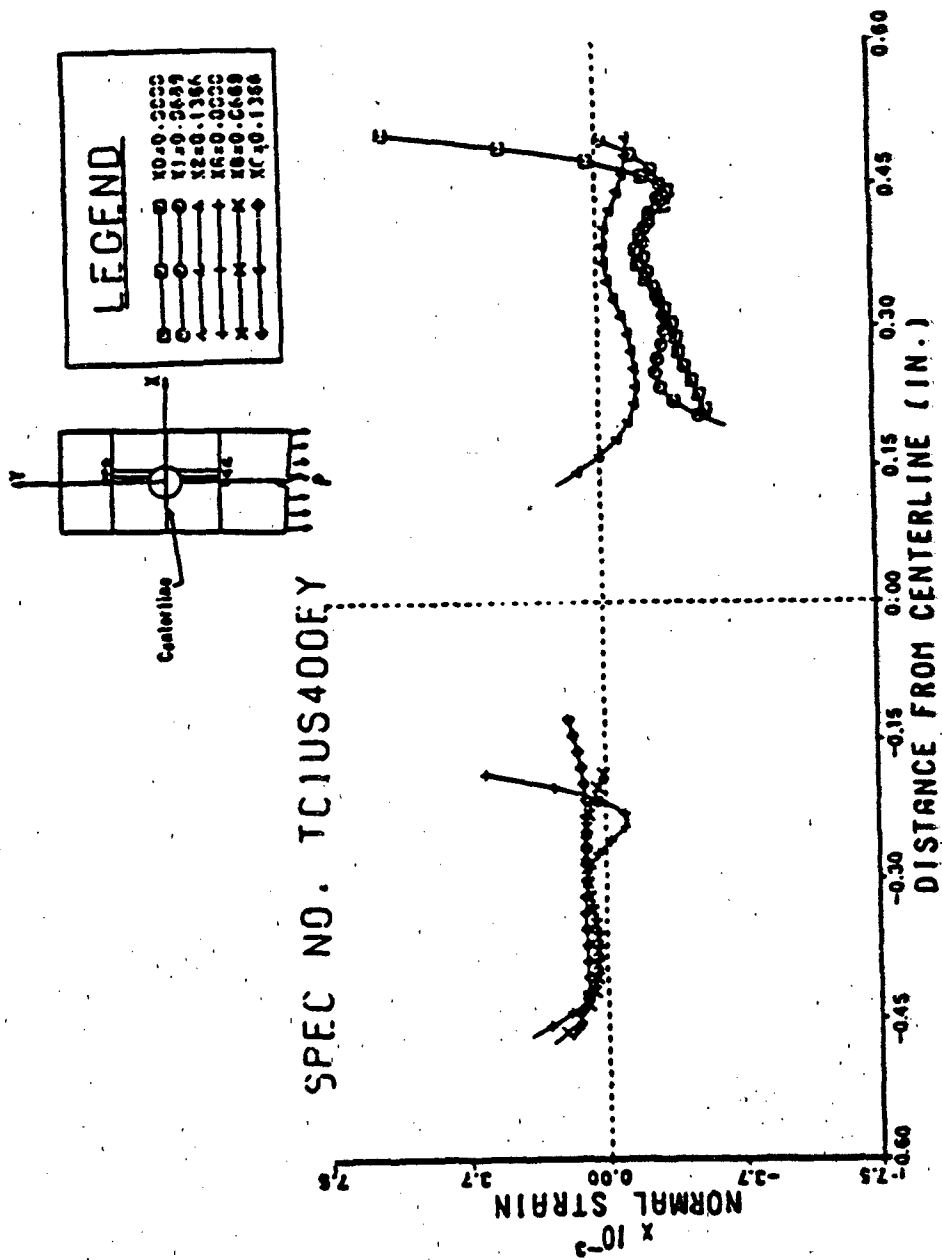
Figure 3-11. Strain parallel to load axis (ϵ_y) along several lines in and opposite to the bearing region.

43

3.8. Experimental Evaluation of Elastic Constants for the Composite

In order to compare theory and experiment, it is necessary to know with precision the material properties of the composite used. An experiment to determine these parameters was conducted.

There are two goals in the design and test of a tensile specimen. First, the existence of a statically determinant, uniaxial state of stress within the test section must be assured; however, producing such a state of stress in the laboratory is not a trivial task. Several analytical studies have revealed that the first goal may be accomplished by establishing the specimen geometry such that the length-to-width ratio is a practical maximum (13, 17, 18). In the current study the maximum length was chosen to be 12 in. and the width one in. The second goal of the design and test of the tensile specimen is to assure that the elastic responses in the in-plane shear and traverse tension modes are constant and that failure will occur within the specimen test section.

Determination of E_1, E_2 and v is quite straight forward. Two tensile tests are required, and for this purpose two specimens were constructed: one with the warp fibers oriented along the direction of the loading (for determination of E_1 and v_{12}) and the other with woven (weft) fibers in the direction of loading (for determination of E_2 and v_{21}).

As shown in Figure 3-12., four single-element strain gages of type EA-13-075AA-120 from Micromeasurements were used to check the uniformity of the stress field. Strain gage rosettes on both faces of the specimen were also used (type CEA-06-062UR-120), first to determine any effect of bending on the specimen and then to obtain the measurements needed to perform the calculations. Effects of transverse sensitivity were checked and found negligible.

The specimens were mounted in a loading frame using grips especially designed to avoid any clamping of the ends and to allow rotations, thus avoiding any end effects.

Every specimen was loaded in increments up to 500 lbs and then unloaded and reloaded to the same stress. The tests were at room temperature (75°F). The strain readings were made with a digital strain indicator from Northern Technical Services, Inc.

Figure 3-13. shows typical plots of stress vs strain obtained from this experiment.

The results obtained for Young's modulus and Poisson's ratio are as follows:

$E_1 = 3.188 \times 10^6$ psi $E_2 = 3.0824 \times 10^6$ psi

$v_{12} = 0.11$ $v_{21} = 0.11$
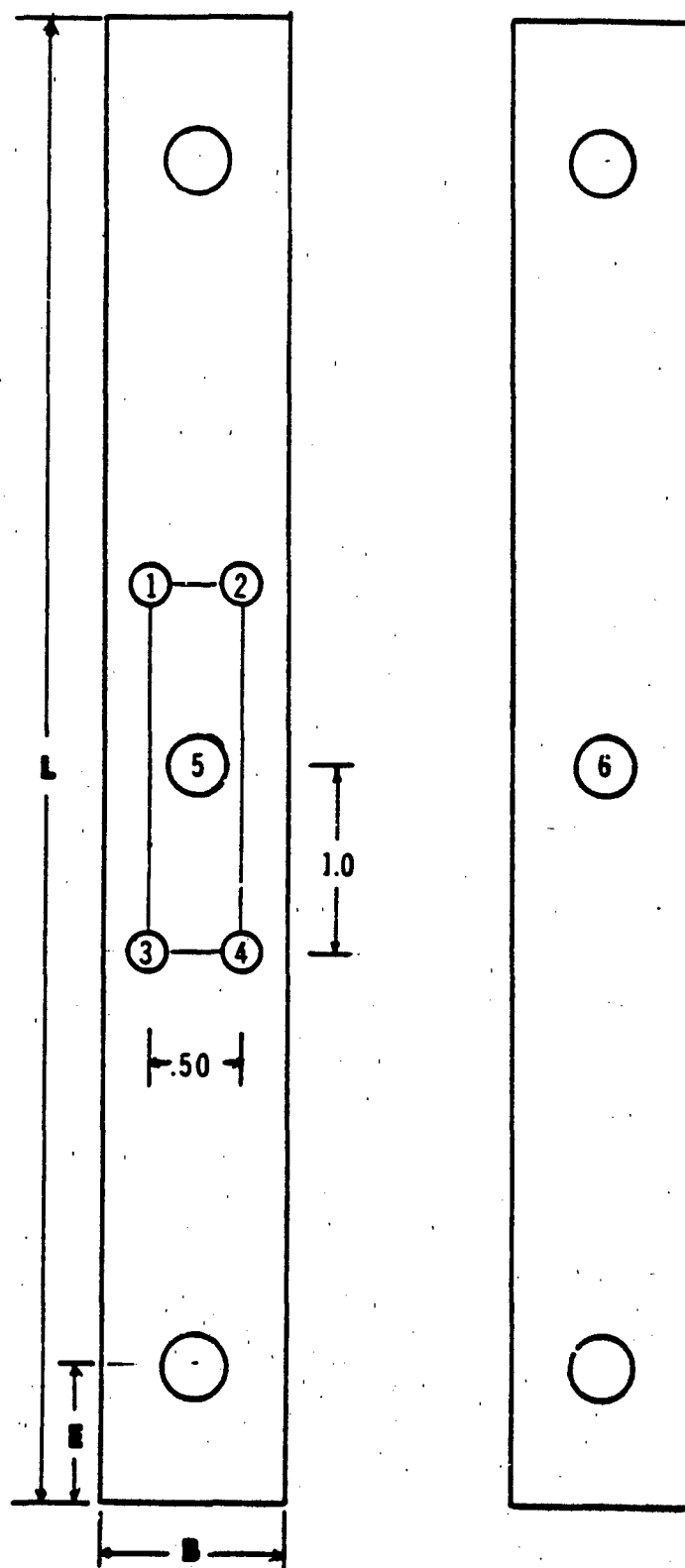
L = 12 IN
B = 1 IN
E = .75 IN

1 - 4 Single element strain gage

5 - 6 Rectangular strain gage rosette

Figure 3-12. Specimen showing location of strain gages.

$E_2 = 3.0824 \times 10^6$

ϵ_2 (μIN/IN)

σ_2 (KSI)

$E_1 = 3.188 \times 10^6$

ϵ_1 (μIN/IN)

σ_1 (KSI)
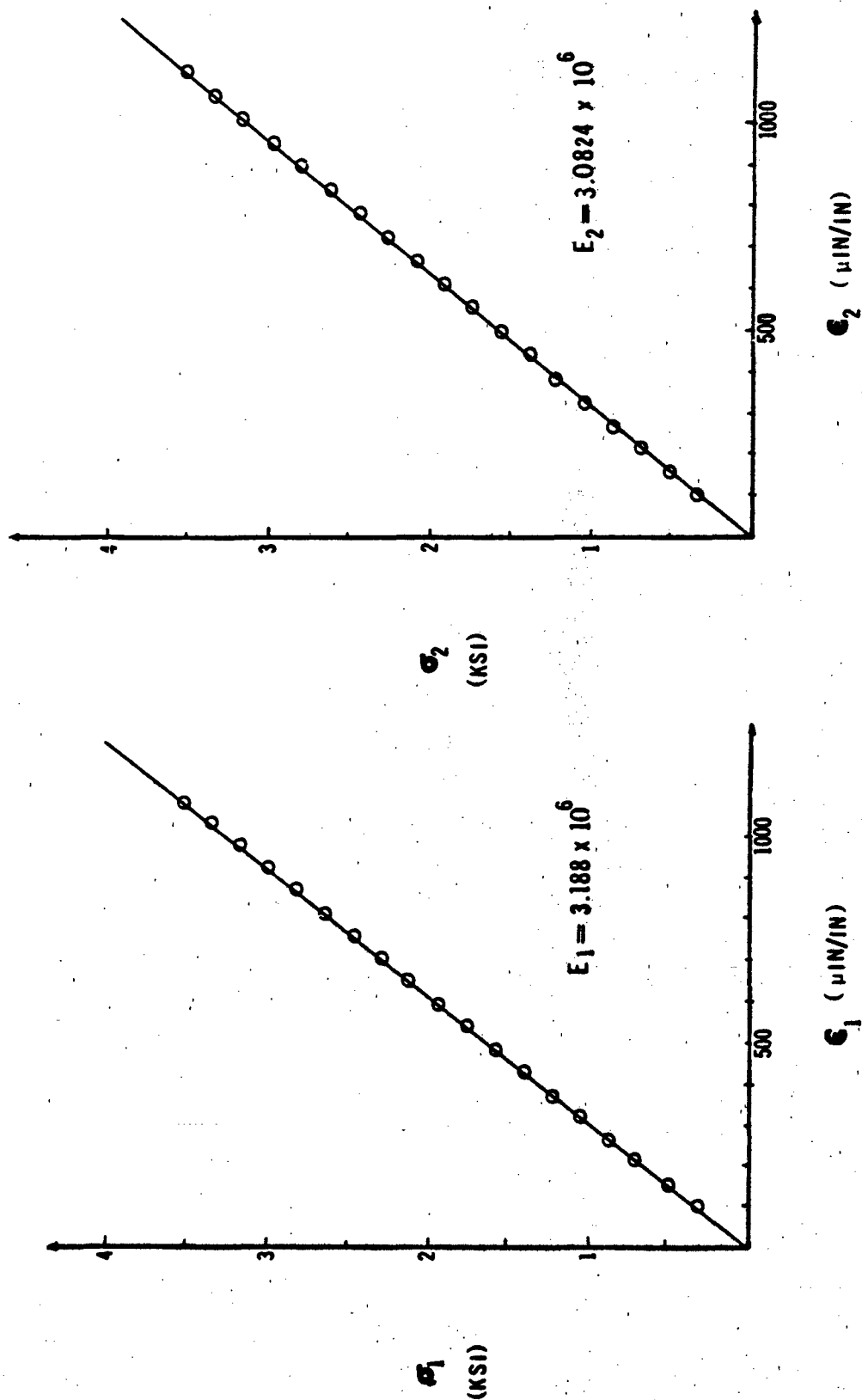
Figure 3-13. Typical tensile stress-strain plots for determination of mechanical properties of orthotropic composite used in this project.

46

A test which is planned for subsequent study is to use an Instron machine to perform the tensile test under different room humidity and room temperatures. It is suspected that humidity and temperature affect the material properties of this specific composite.

3.9 Experimental Results and Discussion

A typical composite pin-loaded joint exhibits a strong coupling between axial strain and bearing capacity at any given pin location.

In this investigation, the specimen had a two-way grating. By using the optical processor, the Moire fringe patterns were formed separately for each direction. One pair (Figures 3-4. and 3-5.) was formed with vertical fringes (direction parallel to the load) and these fringe patterns were used to measure strain ε_x in the traverse direction (perpendicular to the direction of the load). The other pair (Figures 3-6. and 3-7.) were formed with horizontal fringes (perpendicular to the loading direction); fringes in this direction were used to measure strain ε_y in the same direction as the load.

Both the photographs of the horizontally-oriented (from the horizontal grating) fringe patterns and the vertically-oriented (from the vertical grating) fringe patterns yielded some interesting results.

In Figure 3-8. and Figure 3-9., plots of ε_x vs position are shown. In Figure 3-10. and Figure 3-11. ε_y vs position are shown.

From Figures 3-10. and 3-11. we can notice that, in the area of contact between pin and composite, ε_y is highly compressive; but, as we move away from the edge of the hole towards the end of the specimen, its value decreases to an average value.

Now, looking at the right hand edge of the hole, ε_y is of tensile nature; as we move away from the edge of the hole towards the edge of the specimen it decreases to an average value (shown by lines x3 to x7 in Figure 3-11.).

Figure 3-14. shows a distribution of strain based on the results from the the Moire fringes. This figure is developed from Figures 3-10. and 3-11. plus similar strain plots created for additional lines on the specimen.

Much more information useful to the designer can be extracted from these Moire photographs. As an example, examine the areas shown in Figure 3-14. where the normal strain, i.e., ε_y, changes from tensile to compressive. Along that interface, we find a very high shear strain which in some cases can produce delamination and/or failure by shearing, especially along the transition zone from high compressive strain to tensile strain near the fastener. Such features of the Moire results allow the designer to get very useful information anywhere on the surface of the specimen providing better criteria for the determination of the optimum combination of

47
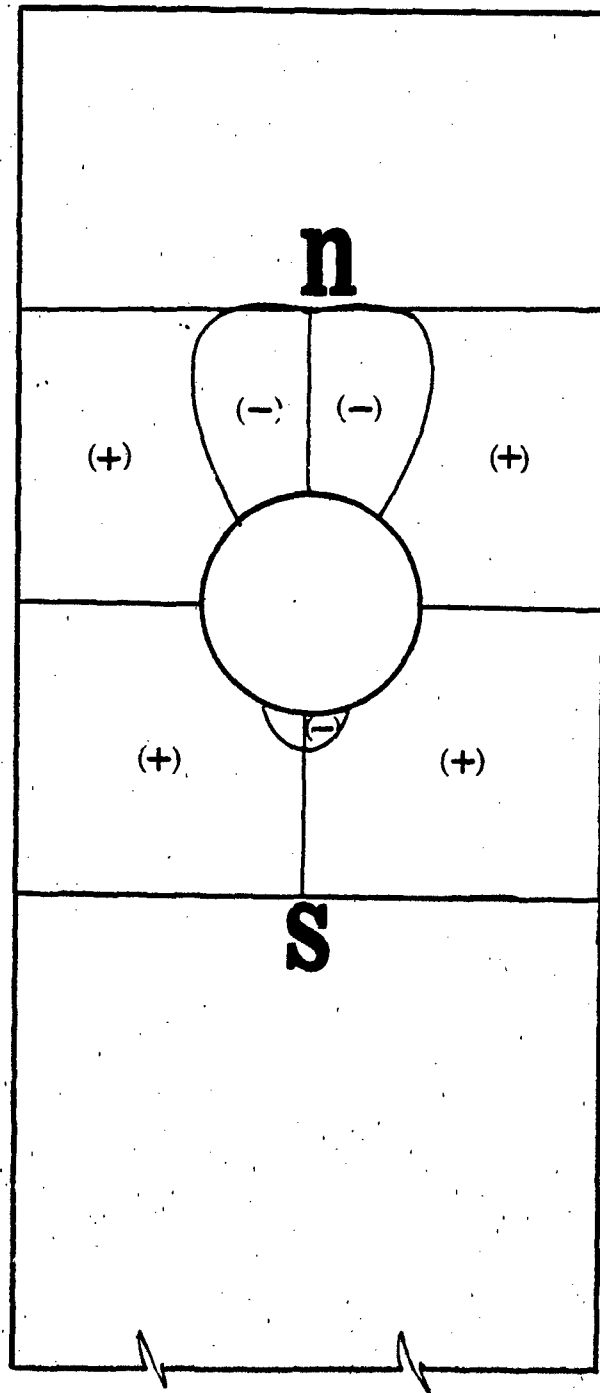
Figure 3-14. Distribution of tensile and compressive strain (ϵ_y) near the fastener hole.

parameters such as distance from hole to edge, ratio of pin to hole
diameters, fiber orientation, lay-up sequence, etc.

3.10. High-sensitivity Interferometric Moire Technique

From the results for ε_x (the smaller strain component), it clear that the
Moire technique has a marginally low strain sensitivity for work on
composite materials. This idea is suggested on Figure 3-8. which shows
poor agreement between values of ε_x at areas located at the right and left
of the specimen (shown by lines x0 to x2 and xA to xC respectively).

The Moire method yields full-field information of the in-plane surface
displacements. It has great potential for the macroscopic strain analysis
of composites, and this method does not suffer any limitation due to
anisotropy, inhomogeneity, or inelasticity of composite material.
Successful Moire strain analysis requires that the sensitivity, which is
governed by the grating frequency, be matched to a degree with the
magnitude of the deformation which is to be measured. Thus an extensive
program to extend the sensitivity by a factor of 10 or more was begun.

An interferometric technique similar to that described by Post (19, 20)
and Walker, Mckelvie and McDonach (21) was developed in this laboratory.
It is evident that this technqiue for measuring the strain distribution
should operate over a sufficiently short gage length to elucidate the
details of the strain distribution, while at the same time giving an
overall picture of the material behavior. In this interferometric Moire
technique, the specimen grating is a phase-type grating. The analysis is
carried out by using overlapping beams of coherent light to create the
specimen grating and the master grating which is projected onto the
deformed specimen.

The particular virtues of the system developed for this investigation
are:

1. The efficiency of light use is very high.

2. No rigid connection is required between the specimen and the
    system. This last feature is relevant in view of the convenience
    of performing measurements in environments which are not so ideal
    as a vibration-free optics laboratory.

3. Measurements car be performed in three different directions,
    yielding a map of strains in the same number of directions and
    allowing calculations of maximum strains. In composites, it does
    not make much sense to talk about principal directions, since
    they depend on the material directions; still, information in
    three directions will provide very useful information for
    specific situations of fastener design.

Preliminary testing of this technique has been conducted and the results
appear to be very promising. Figures 3-15. and 3-16. show Moire fringes

49
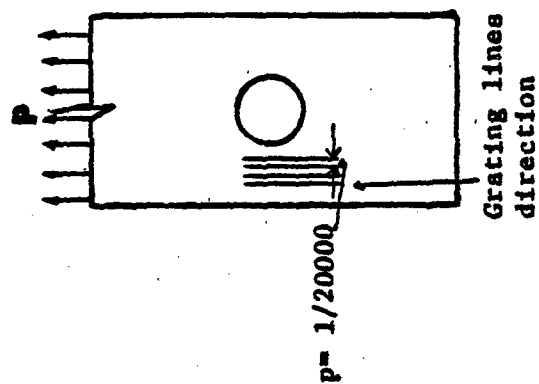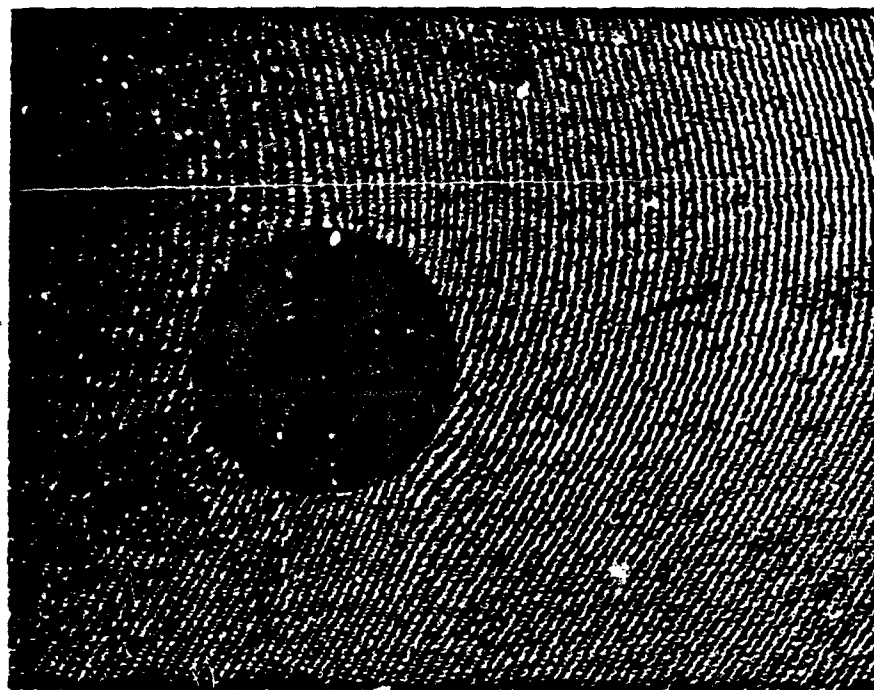
Figure 3-15. High sensitivity Moire fringes
showing displacements perpendicular to the direction
of loading for no load with rotational mismatch.
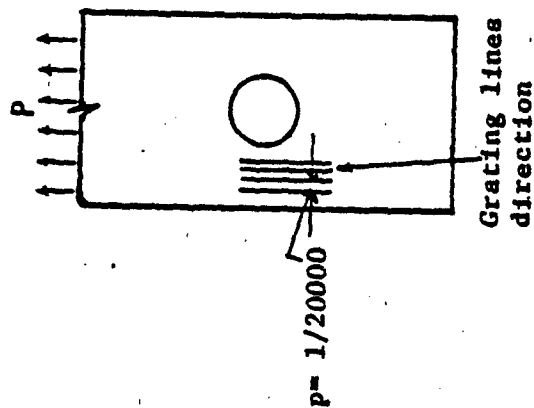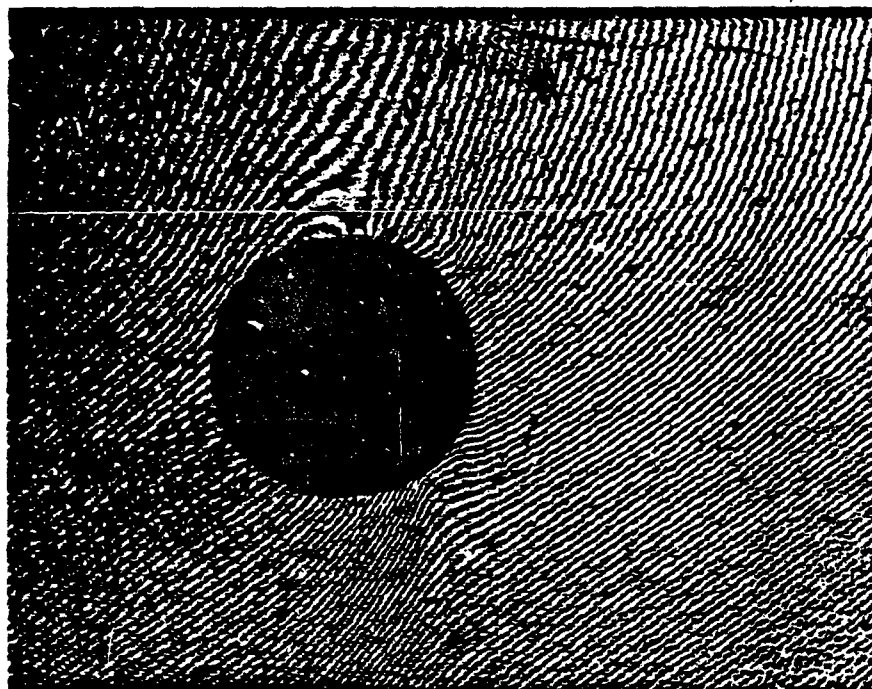
Figure 3-16. High sensitivity Moire fringes showing displacements perpendicular to the direction of loading for a 130 lb. load with rotational mismatch.

of displacement in the x-direction (perpendicular to the direction of the loading). Notice the difference between these fringe patterns and those obtained by the traditional Moire technique (Figures 3-4. and 3-5.).

4.0. COMPARISON BETWEEN EXPERIMENTAL AND NUMERICAL RESULTS

Section 3 describes the methodology of obtaining strain in the actual composite material by Moire techniques which are self-calibrating and which do not depend on assumptions of material behavior. Typical results are reported. Section 2 described a boundary-element approach to the problem and gives results from that method. Some finite element results are also computed and used for comparison of the two numerical approaches.

It is instructive and valuable to designer, theoretician, and experimentalist to compare the results from these widely diverse approaches to the problem. Since the methods are so different, good agreement of results would imply that the results are probably correct. Disagreement would give an idea of the magnitudes of errors in either or both sets of results.

To perform the comparison, some strains measured by Moire were converted to stress by use of generalized Hooke's law. This procedure inserts an assumption of material behavior into the experimental findings, but it does facilitate comparison. It is probably more reasonable, but also more difficult, to use Hooke's law to convert the numerical results to strain. The conversion of experimental data was carried out for ϵ_y at selected points along the ligament line between hole boundary and specimen edge. These stresses were normalized, then plotted. They are compared with the matching finite element values. The comparison is shown graphically in Figure 4-1. The agreement between numerical and experimental findings is excellent, especially when one considers the fact that these composites do show some nonhomogeneity, i.e., properties vary slightly from point to point.

This comparison is not extensive, but it does indicate that the work and the results are probably correct. Comparisons for other critical areas of the stress field are planned. In addition, it would be advisable to obtain a measure of the inhomogeneity of the material so that a "scatter band" of expected stress for a given load situation can be established. The results presented suggest that numerical and experiment results would both lie within any such scatter band.
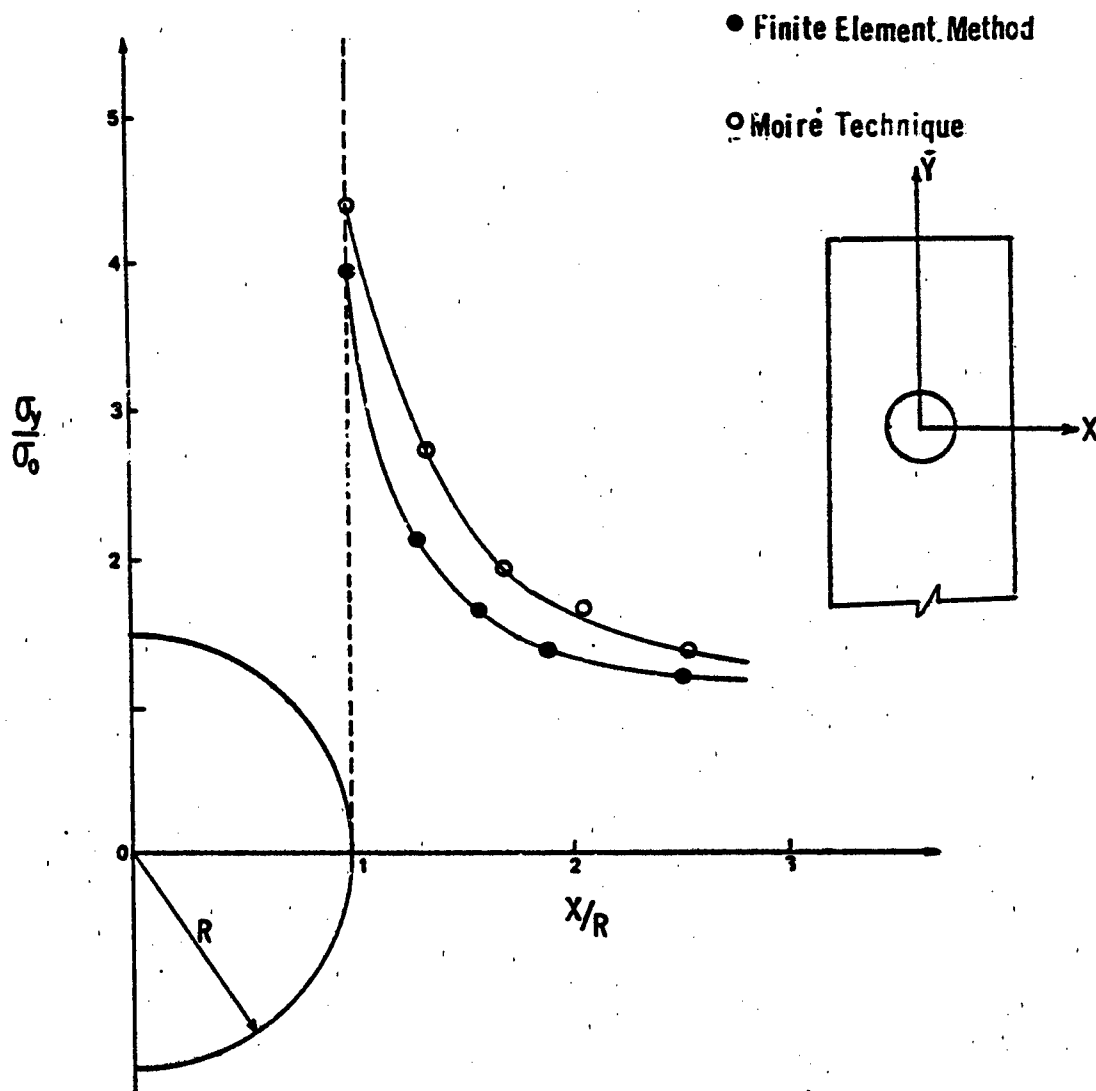
Figure 4-1. Comparison of stress concentration factors obtained by numerical and experimental techniques.

REFERENCES

1. C.A. Brebbia (ed), Proceeding of the 3rd International seminar on Boundary Element Methods, Pub. Springer-Verlag, 1981.

2. N.J. Altiero and D.L. Sikarskie "An Integral Equation Method Applied to Penetration Problems in Rock Mechanics," Boundary Integral Equation Method: Computational Applications in Applied Mechanics, AMD-Vol. II, ASME, 1975, 119-141.

3. C.G. Harris and W.B. Evans, "Extension of Numerical Quadrature Formula to Cater for End Point Singular Behavior Over Finite Integrals," Intern. J. Computer Math. 68, 1977, 219-277.

4. R.E. Peterson, Stress Concentration Factors, John Wiley, 1974.

5. Cloud, G., "Simple Optical Processing of Moire-grating Photographs," E.p. Mech., 20, 8, 265-272 (Aug. 1980).

6. G. Cloud, Radke, R., and Peiffer, J. "Moire Gratings for High Temperatures and Long Times," Exp. Mech. Vol. 19, No. 10, 19N-21N. Oct. 1979.

7. Cloud, G., Paleebut, "The Dimensional Nature of Strain Field Near Coldworked Holes." AFWAL-TR-80-4204, Wright-Patterson AFB, Ohio (1980).

8. Paleebut, Somnuek, "An Experimental Study of Three-dimensional Strain Around Cold Worked Holes and in Thick Compact Tension Specimens," Ph.D. Thesis, Michigan State University, Department of Metallury, Mechanics and Materials Science, 1982.

9. Cloud, G., "Residual Surface Strain Distributions Near Holes Which are Cold Worked to Various Degrees," Technical Report AFML-TR-78-153, Wright-Patterson AFB, Ohio (1980).

10. Cloud, G., "Measurement of Strain Fields Near Cold Worked Holes," Experimental Mechanics, 20, 2, 9-16, (January 1980).

11. Cloud, G., and Sulaimana, R., "An Experimental Study of Large Compressive Loads Upon Residual Strain Fields and the Interaction Between Surface Strain Fields Created by Cold Working Fastener Holes," Technical Report AFML-TR-80-4206, Wright-Patterson AFB, Ohio (1980).

12. Cloud, G., and Tipton, M., "An Experimental Study of the Interaction of Strain Fields Between Coldworked Fastener Holes," Technical Report, AFML-TR-80-4205, Wright-Patterson AFB, Ohio (1980).

13. Horgan C.O., "Saint-Venant End Effects in Composites," Journal of Composite Materials, Vol. 16, Sept. 1982 pp. 411.

14. Luxmoore, A. and Hermann, R., "An Investigation of Photoresists For Use in Optical Strain Analysis," Jrnl. of Strain Anal., 5, 3, 162 July 1970.

15. Holister, G.S., and Luxmoore, A.R. "The Production of High density Moire Grids," Exp. Mech. 8, 210, May 1968.

16. Luxmoore, A.R., and Hermann R., "The Rapid Deposition of Moire Grids," Exp. Mech, 11, 5, 375, August 1971.

17. Pagano, N.J., and Halpin, J.C., "Influence of End Constraint in the Testing of Anistropic Bodies," J. Composite Materials, Vol. 2 (1969) p. 18.

18. R.B. Pipes., "On the Off-Axis Strength Test for Anisotropic Materials," Journal of Composite Materials, Vol. 7 (April 1973), p. 246.

19. Post, D., "Optical Interference for Deformation Measurements-Classical, Holographic and Moire' Interferometry" Mechanics of Nondestructive Testing Proceedings edited by W.W. Stinchcomb, Plenum Publishing Corp., NY (1980).

20. Post, D. and Baracat, W.A., "High Sensitivity Moire Interferometry--A Simplified Approach," Exp. Mech. 21, 3, 100-104 (March 1981).

21. McDonach, A., McKelvie, J., Mackenzie, P., and Walker, C.A., Proceedings of the V International Congress on Experimental Mechanics, Montreal, Canada June 10-15,1984 pp. 308-313.

This page left blank intentionally.

APPENDIX A

FUNDAMENTAL SOLUTIONS

This page left blank intentionally.

For the isotropic case

The stress and displacement fields at a point (x,y) due to a unit point load acting at the origin of coordinates in the x-direction in an infinite plate with material properties G and ν under plane stress are:

$$
\begin{Bmatrix}
4G\ U_x \\[4pt]
4G\ U_y \\[4pt]
H_{xx} \\[4pt]
H_{xy} \\[4pt]
H_{yy}
\end{Bmatrix}
= -\frac{1+\nu}{2\pi}
\begin{Bmatrix}
Q\ \ln r^2 + y^2/r^2 \\[4pt]
-xy/r^2 \\[4pt]
x(P + x^2/r^2)/r^2 \\[4pt]
y(P + x^2/r^2)/r^2 \\[4pt]
x(-P + y^2/r^2)/r^2
\end{Bmatrix}
$$

where $P = (1-\nu)/2(1+\nu)$, $Q = .5 + 2P$ and $r^2 = x^2 + y^2$. For a unit load in the y-direction, the results are:

$$
\begin{Bmatrix}
4G\ U_x \\[4pt]
4G\ U_y \\[4pt]
H_{xx} \\[4pt]
H_{xy} \\[4pt]
H_{yy}
\end{Bmatrix}
= -\frac{1+\nu}{2\pi}
\begin{Bmatrix}
-xy/r^2 \\[4pt]
Q\ \ln r^2 + x^2/r^2 \\[4pt]
y(-P + x^2/r^2)/r^2 \\[4pt]
x(P + y^2/r^2)/r^2 \\[4pt]
y(P + y^2/r^2)/r^2
\end{Bmatrix}
$$

The tractions are:

$$T_{x,k} = H_{xx,k}\cos\alpha + H_{xy,k}\sin\alpha$$

$$T_{y,k} = H_{xy,k}\cos\alpha + H_{yy,k}\sin\alpha$$

where k = either x or y and α = angle that the exterior normal makes with the x-axis.

For the orthotropic case

For a unit load in the x-direction

A-3

$$U_{xx} \qquad (c_1 A_1 \ln r_2 - c_3 A_2 \ln r_1)/2$$

$$U_{yx} \qquad A_1 A_2 (\phi_1 - \phi_2)/c_{22}$$

$$H_{xxx} \qquad = k \qquad (c_1 r_2 - c_3 r_1)x$$

$$H_{xyx} \qquad (c_1 r_2 - c_3 r_1)y$$

$$H_{yyx} \qquad (\delta_1 c_3 r_1 - \delta_2 c_1 r_2)x$$

For a unit load in the y-direction

$$U_{xy} \qquad A_1 A_2 (\phi_1 - \phi_2)/c_{22}$$

$$U_{yy} \qquad (c_4 A_1 \ln r_1 - c_2 A_2 \ln r_2)/2$$

$$H_{xxy} \qquad = k \qquad (c_2 r_2 - c_4 r_1)y$$

$$H_{xyy} \qquad (\delta_1 c_4 r_1 - \delta_2 c_2 r_2)x$$

$$H_{yyy} \qquad (\delta_1 c_4 r_1 - \delta_2 c_2 r_2)y$$

with

$$k = 1/2\pi(\delta_2 - \delta_1),$$

$$r_i = 1/(\delta_i x^2 + y^2), \quad i=1,2$$

$$A_i = c_{12} - \delta_i c_{22}, \quad i=1,2$$

$$\phi_1 - \phi_2 = \sin^{-1}[yx\sqrt{r_1 r_2}\,(\sqrt{\delta_2} - \sqrt{\delta_1})],$$

$$c_1 = \sqrt{\delta_2}\,(\delta_1 - c_{12}/c_{22}),$$

$$c_2 = \sqrt{\delta_2}\,(1 - \delta_1 c_{12}/c_{11}),$$

$$c_3 = \sqrt{\delta_1}\,(\delta_2 - c_{12}/c_{22}),$$

$$c_4 = \sqrt{\delta_1}\,(1 - \delta_2 c_{12}/c_{11}),$$

δ_1 and δ_2 are the roots of the characteristic equation of the material;

$$c_{22}\,\delta^2 - (2c_{12} + c_{33})\delta + c_{11} = 0$$

Note that δ's are either real or complex. If they are real, then since $\delta_1 \delta_2 = c_{11}/c_{12} > 0$, they are either both positive or both negative. For clearness, the δ's are taken to be real. For complex δ's, δ_2 is necessarily the conjugate of δ_1 and the c's obtained above are substituted in (11) to obtain the equivalent complex forms of the fundamental solution, the real parts of which represent U's and H's.

APPENDIX B

THE COMPUTER PROGRAM "BEM"

This page left blank intentionally.

Major steps in constructing BEM computer program

Step 1. Provide the following data:

      Boundary points coordinator (XB, YB)

      The angles that outward normal at boundary nodes make with +x-axis (T)

      Field points coordinates (XF,YF)

      Boundary conditions in X and Y (BC),
         BC = 0 displacement prescribed
         BC = 1 stress prescribed

      Boundary values (B)

      Integration nodes and weights (Z,W)

      Compliances (c's)

Step 2. Construct the influence matrix, A

Step 3. Solve AX = B
       (stores results in B)

Step 4. Calculate displacements and stresses at given field points

Remark:

The computer program BEM is developed for real δ_1 and δ_2. The complex version of BEM follows directly from the discussion given in Appendix I.

```fortran
      PROGRAM BEM(INPUT,OUTPUT)
C     ***********************************************************************
      PARAMETER(N=60,N2=2*N,M=26)
      REAL XB(N+1),YB(N+1),T(N),XF(M),YF(M),BC(N2),A(N2,N2),B(N2),
     +Z(4),W(4)
      READ*, C11,C12,C22,C33
      READ*,(Z(I),I=1,4),(W(I),I=1,4)
      READ*,(XB(I),YB(I),I=1,N),(T(I),I=1,N)
      READ*, (BC(I),I=1,N2),(B(I),I=1,N2)
      READ*,(XF(I),YF(I),I=1,M)
      PI=3.141592653589
C     COMPUTE CONSTANTS IN THE FUNDAMENTAL SOLUTIONS
      P1=(C12+.5*C33)/C22
      X1=P1-SQRT(P1*P1-C11/C22)
      X2=2.*P1-X1
      X3=SQRT(X2)-SQRT(X1)
      CN=2.*PI*(X2-X1)
      A1=C12-X1*C22
      A2=C12-X2*C22
      C1=(X1-C12/C22)*SQRT(X2)
      C2=(1.-X1*C12/C11)*SQRT(X2)
      C3=(X2-C12/C22)*SQRT(X1)
      C4=(1.-X2*C12/C11)*SQRT(X1)

C     CONSTRUCT THE INFLUENCE MATRIX, A
      DO 100 I=1,N
      I1=2*I-1
      I2=2*I
      CT=COS(T(I))
      ST=SIN(T(I))
      FX=.5*(XB(I+1)+XB(I))
      FY=.5*(YB(I+1)+YB(I))
      DO 100 J=1,N
      AX=XB(J+1)-XB(J)
      AY=YB(J+1)-YB(J)
      H=SQRT(AX*AX+AY*AY)
      QI=-.5*H*(ALOG(.5*H)-1.)
      IF (I.EQ.J) GOTO 50
      UXX=UXY=UYY=HXXX=HXYX=HYYX=HXXY=HXYY=HYYY=0.
      DO 7 K=1,4
      X=FX-AX*Z(K)-XB(J)
      Y=FY-AY*Z(K)-YB(J)
      R1=1./(X1*X*X+Y*Y)
      R2=1./(X2*X*X+Y*Y)
      UXX=UXX+.5*(C1*A1*ALOG(R2)-C3*A2*ALOG(R1))*H*W(K)
      UXY=UXY+A1*A2*ASIN(X*Y*X3*SQRT(R1*R2))/C22*H*W(K)
      HXXX=HXXX+(C1*R2-C3*R1)*X*H*W(K)
      HXYX=HXYX+(C1*R2-C3*R1)*Y*H*W(K)
      HYYX=HYYX+(X1*C3*R1-X2*C1*R2)*X*H*W(K)
      HXXY=HXXY+(C2*R2-C4*R1)*Y*H*W(K)
      HXYY=HXYY+(X1*C4*R1-X2*C2*R2)*X*H*W(K)
    7 HYYY=HYYY+(X1*C4*R1-X2*C2*R2)*Y*H*W(K)
      IF(BC(I1).EQ.0.) GOTO 10
      A(I1,2*J-1)=HXXX*CT*CT+HYYX*ST*ST+2.*HXYX*CT*ST
      A(I1,2*J)=HXXY*CT*CT+HYYY*ST*ST+2.*HXYY*CT*ST
      GOTO 20
   10 A(I1,2*J-1)=UXX*CT+UXY*ST
      A(I1,2*J)=UXY*CT+UYY*ST
   20 IF(BC(I2).EQ.0.) GOTO 30
      A(I2,2*J-1)=(HYYX-HXXX)*CT*ST+HXYX*(CT*CT-ST*ST)
      A(I2,2*J)=(HYYY-HXXY)*CT*ST+HXYY*(CT*CT-ST*ST)
      GOTO 100
   30 A(I2,2*J-1)=UXY*CT-UXX*ST
      A(I2,2*J)=UYY*CT-UXY*ST
      GOTO 100
   50 A(I1,2*J-1)=.5*CN*(BC(I1))*CT+(1.-BC(I1))*QI*(C1*A1-C3*A2)*CT
      A(I1,2*J)=.5*CN*BC(I1)*ST+(1.-BC(I1))*QI*(C1*A1-C3*A2)*ST
      A(I2,2*J-1)=-.5*CN*BC(I2)*ST+(1.-BC(I2))*QI*(C2*A2-C4*A1)*ST
      A(I2,2*J)=.5*CN*(BC(I2))*CT+(1.-BC(I2))*QI*(C4*A1-C2*A2)*CT
  100 CONTINUE
C
C     SOLVE A.X = B
      CALL MATX(N2,A,B)
      PRINT 500
```

```
C      CALCULATE DISPLACEMENTS AND STRESSES AT GIVEN FIELD POINTS
       DO 300 I=1,M
       UX=UY=TXX=TXY=TYY=0.
       CT=COS(T(I))
       ST=SIN(T(I))
       DO 200 J=1,N
       K=2*J
       AX=XB(J+1)-XB(J)
       AY=YB(J+1)-YB(J)
       H=SQRT(AX*AX+AY*AY)
       IF((XF(I)-.5*(XB(J+1)+XB(J)))**2+(YF(I)-.5*(YB(J+1)+YB(J)))**2.
      *LE.1.E-8) GOTO 150
       DO 110 L=1,4
       X=XF(I)-AX*Z(L)-XB(J)
       Y=YF(I)-Z(L)*AY-YB(J)
       R1=1./(X1*X*X+Y*Y)
       R2=1./(X2*X*X+Y*Y)
       UXX=.5*(C1*A1*ALOG(R2)-C3*A2*ALOG(R1))
       UXY=A1*A2*ASIN(X*Y*X3*SQRT(R1*R2))/C22
       UYY=.5*(C4*A1*ALOG(R1)-C2*A2*ALOG(R2))
       HXXX=(C1*R2-C3*R1)*X
       HXYX=(C1*R2-C3*R1)*Y
       HYYX=(X1*C3*R1-X2*C1*R2)*X
       HXXY=(C2*R2-C4*R1)*Y
       HXYY=(X1*C4*R1-X2*C2*R2)*X
       HYYY=(X1*C4*R1-X2*C2*R2)*Y
       UX=UX+(B(K-1)*UXX+B(K)*UXY)*H*W(L)
       UY=UY+(B(K-1)*UXY+B(K)*UYY)*H*W(L)
       TXX=TXX+(B(K-1)*HXXX+B(K)*HXXY)*H*W(L)
       TXY=TXY+(B(K-1)*HXYX+B(K)*HXYY)*H*W(L)
       TYY=TYY+(B(K-1)*HYYX+B(K)*HYYY)*H*W(L)
110    CONTINUE
       GOTO 200
150    QI=-H*(ALOG(H)-1.)
       UXX=QI*((C1*A1-C3*A2)*CT**2+(C4*A1-C2*A2)*ST**2)
       UXY=QI*(C1*A1+C2*A2-C3*A2-C4*A1)*CT*ST
       UYY=QI*((C1*A1-C3*A2)*ST**2+(C4*A1-C2*A2)*CT**2)
       UX=UX+UXX*B(K-1)+UXY*B(K)
       UY=UY+UXY*B(K-1)+UYY*B(K)
       TXX=TXX+.5*CN*(CT*B(K-1)-ST*B(K))
       TXY=TXY+.5*CN*(-CT*B(K-1)+ST*B(K))
       TYY=TYY+.5*CN*(ST*B(K-1)+CT*B(K))
200    CONTINUE
300    PRINT 400, I,XF(I),YF(I),UX,UY,TXX,TXY,TYY
400    FORMAT (1H0,5X,I2,3X,2(4X,F8.4),6X,2(4X,F12.8),6X,3(4X,F12.8))
500    FORMAT('0',5X,'NO',T21,'X',T32,'Y',T52,'UX',T68,'UY'
      *,T90,'TXX',T106,'TXY',T122,'TYY'/)
       END
*EOR
C      INPUT DATAS
*EOF
```

This page left blank intentionally.

APPENDIX C

SIMPLE OPTICAL PROCESSING OF
MOIRE-GRATING PHOTOGRAPHS

This page left blank intentionally.

Simple Optical Processing of Moiré-grating Photographs

Paper explains and illustrates how a few basic
optical concepts can be employed in simple ways to improve
sensitivity and quality of moiré measurements

by Gary L. Cloud

ABSTRACT—The three fundamental optical phenomena of
diffraction, two-beam interference, and transformation by a
lens form the basis of modern moiré strain-measurement
techniques. The improved understanding of diffraction by
superimposed gratings and optical spatial filtering leads to a
general gain of freedom in designing moiré experiments.
Benefits characteristic of refined but very simple optical-
data-processing techniques include greater sensitivity, less-
demanding procedure, possible large gains in sensitivity, and
the ability to choose certain moiré parameters, such as
sensitivity, after an experiment is concluded and the raw data
stored. Sample results from a study of strains near cold-
worked holes demonstrate that acceptable results can be had
with elementary apparatus and systematic exploitation of
optical-data processing.

Introduction

The use of various techniques of optical-data pro-
cessing in moiré measurement of deformation and strain
is neither new nor profound. It seems, however, that
benefits derivable from these methods, as well as their
basic concepts, are not well understood by many practi-
tioners of experimental mechanics, whose training and
experience are likely in mechanics and engineering
instead of in physics. Physicists might share some blame
for this condition, because their presentation of the
subject often is obscurely mathematical and devoid of
examples of practical range of physical phenomena. A
result is that experimental methods having much power
are not exploited to any substantial degree; and one still
hears talk of basic sensitivity limitations of moiré methods
and of requirements for refined and expensive apparatus,
including sharp gratings of high spatial frequency. In
fact, these limitations are no longer very important. One
is largely free to choose and design a moiré procedure to
fit a given problem and laboratory situation. The con-
tinuing development of sophisticated optical devices
combines with our increasing maturity in understanding
optical phenomena to yield further gains of freedom
and power in measurement technique.

Gary L. Cloud (SESA Member) is Professor, Department of Metallurgy,
Mechanics and Materials Science, Michigan State University, East
Lansing, MI 48824.

Original manuscript submitted: January 26, 1979. Final version received:
February 19, 1980.

This paper has the purpose of drawing together and
explaining without mathematics the physical phenomena
which are important in optical-data processing of moiré-
grating photographs to obtain fringe patterns having
sensitivity multiplication, pitch mismatch, and, more
important, the possibility of choosing certain moiré
parameters after an experiment is finished and the data
are stored. An example of such a measurement exercise is
included.

Classification of Moiré Techniques

The several approaches to creating useful moiré fringes
may be divided for convenience of thinking into the
following categories:

(1) Direct superimposition of master and specimen
gratings by placing them into physical contact for sub-
sequent observation or storage of the fringe pattern.

(2) Using optical imaging to indirectly superimpose
gratings on a ground glass, in a camera, on a film, or on a
partial mirror for real-time observation or storage, such
as by double-exposure photography, of the fringe patterns.

(3) Direct superimposition of stored replicas (photo-
graphic or transfer grids) of the specimen and master
gratings with storage or observation of the fringes.

(4) Superimposition of stored replica master and
specimen gratings with optical-data processing and optical
imaging to create a fringe pattern for observation or
storage.

(5) Certain combinations of the above.

Although useful moiré-fringe patterns can be obtained
by the direct superimposition methods, such simple
procedures do not yield the best results. It is in the
approaches which are conceptually simplest that the most
highly refined apparatus is needed to procure an acceptable
product; only a small portion of the information which
might be contained in a grating photograph is used; and
the classical limitations on moiré sensitivity become
important.

Increased exploitation of available stored data, better
sensitivity, and more control of the measurement process
can be had by utilizing only a few basic concepts and
simple procedures in optical-data processing.

Three Fundamental Concepts

There are just three phenomena which form the basis

for optical manipulation of grating replicas to obtain
moiré interference-fringe maps. These concepts are
described below.

Two-beam Interference

Two-component beams from a single source such as a
laser or single-point source can traverse different paths
and then be recombined to produce interference fringes.
Figure 1 shows this effect for two plane waves. The fringe
spacing on the screen is directly related to the angle
between the beam axes, the tilt of the screen, and the
nature of the two beams. The situation of greatest interest
is when two coherent beams intersect at a small angle. It
is easy to show that two intersecting beams will produce a
pattern of interference fringes in space which are made
visible by inserting a screen or optical system into the
area of intersection.

Diffraction by Grating

Part of the light passing through or reflected from a
grating will be deviated from its original path by an
amount dependent on the grating spatial frequency, the
wavelength of light and the incidence angle. Figure 2(a)
illustrates this behavior for a simple sine grating, where a
normally incident beam is divided into three parts. More
complex gratings, such as the bar and space type shown
in Fig. 2(b), can be thought of as the sum of several sine
gratings. A pair of diffracted beams will be produced for
each of the component higher-frequency sine gratings. It
appears, and correctly, that the diffraction pattern gives a
direct indication of the Fourier components of the
diffraction grating.

The Lens as a Fourier Transformer

A simple lens acts as a whole-field optical Fourier
transforming device. If light with sufficient coherence
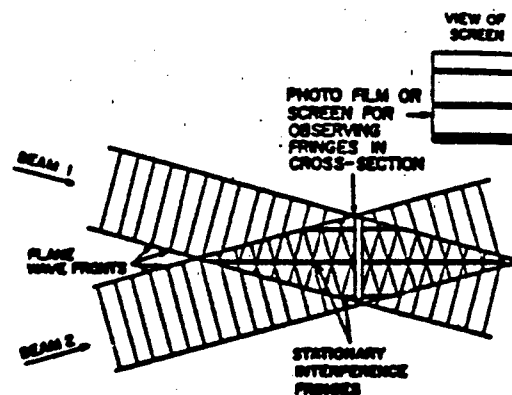
Fig. 1—Interference of two coherent collimated intersecting beams

potential (and usually collimated) is passed through some
spatial signal (transparency) and then through a lens
(order of elements can be reversed), a light distribution
which is directly and simply related to the Fourier trans-
form of the input signal will be observed in the back focal
plane of the lens. This plane is found most easily by
locating the spot where all the light is focused when the
input transparency is not in place. Figure 3 shows a
typical arrangement. It is important to keep in mind that
distance in the transform plane corresponds to spatial
frequency in the input plane. The light distribution gives
a visual picture of the spatial-frequency content of the
input. That is, a lens is a spatial-frequency analyzer.

Purists might hasten to point out that the two previous
concepts—"two-beam interference" and "diffraction by
grating"—are really only slightly different manifestations

Fig. 2—Diffraction of narrow light beam by: (a) sine grating; (b) bar-space grating

C-4
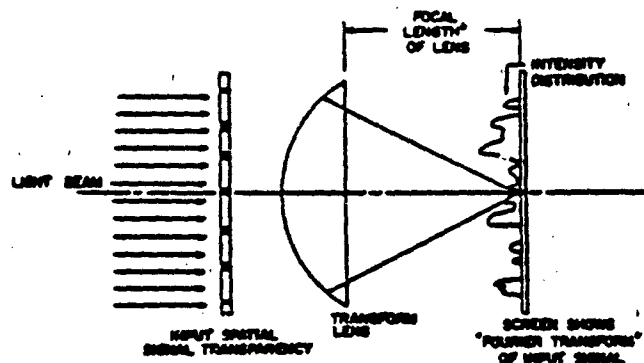
Fig. 3—Creation of optical Fourier transform of input-signal transparency

* ACTUALLY DISTANCE TO BACK FOCAL PLANE FOR THE GIVEN LIGHT BEAM=FOCAL LENGTH FOR COLLIMATED BEAM

of a single physical phenomenon—that being diffraction at an aperture. Such thinking is correct, but it is not especially useful. Separating the concepts allows one to look at the optical processing of grating photographs from two different points of view.

Diffraction by Superimposed Gratings

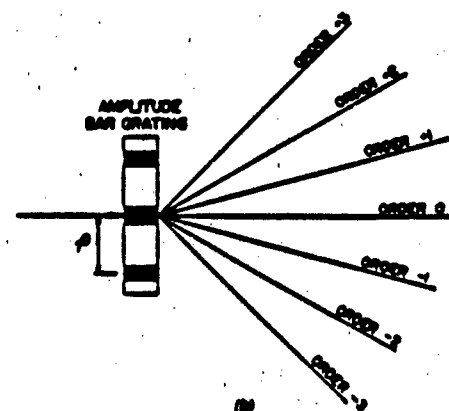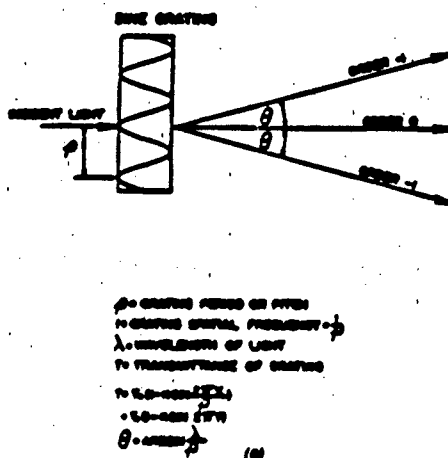The theory of moiré-fringe formation by superimposing two diffraction gratings of nearly equal spatial frequencies and orientations has been presented in elegant detail by Guild.[1] His ideas were extended, refined, and demonstrated within the context of moiré strain analysis in a series of definitive papers by Post[2] and by Post and

McLaughlin[3] as well as by Holister.[4] The exposition below draws heavily from Post's fine explanations.

It is assumed that the experimenter has created by some process, probably photographic, two grating transparencies. One of these might be a replica of a master grating, and the other is probably a recording of a distorted specimen grating. The quantity of interest is, of course, the degree and direction of distortion of the second grating. In moiré analysis, the procedure is to superimpose these gratings somehow to produce a high-contrast pattern of interference fringes which is easily observed and photographed and which has optimum properties for subsequent analysis in order to obtain displacement and strain maps.

Fig. 4—Formation of two-beam interference fringes by light diffracted through two fine gratings having slightly different spatial frequencies

INTERFERENCE FRINGES CAN BE VIEWED IN SMALL SCALE ON SCREEN OR CAN BE IMAGED IN LARGE SCALE BY CAMERA

C-5

The formation and meaning of the fringes produced by passing light through the two diffraction gratings can be understood by calling upon two of the basic concepts outlined above.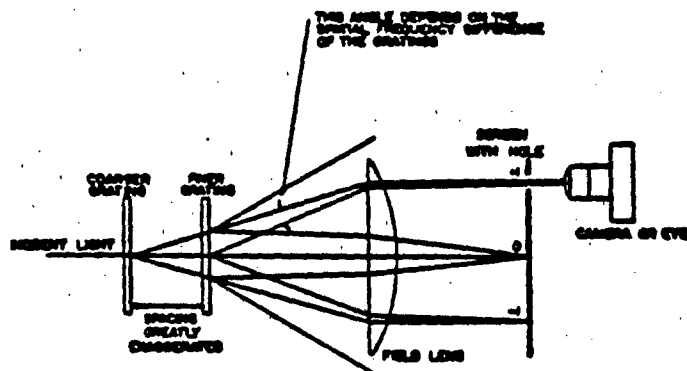 If a single narrow beam of light is made to pass normally (normal incidence chosen for convenience) through (or reflect from) a sinusoidal amplitude or phase grating, the beam will be divided into three parts at the grating, as was illustrated in Fig. 1. The first part, called the zero order, is the undisturbed portion of the beam which passes directly through the grating. The other two parts, called first orders, deviate symmetrically from the zero order.

Now, consider what happens when a narrow collimated beam passes through two sinusoidal gratings of slightly different spatial frequencies, as illustrated in Fig. 4. Five distinct beam groups will appear in this case. The center group is an attenuated version of the incident beam. The extreme orders each contain only a single component which has been diffracted by each of the two gratings in succession. The intermediate beam groups numbered +1 and -1 are the ones of interest. They each contain two beams, the first has been diffracted at the first grating only, and the second has been diffracted at the second grating. These two beams in the group are nearly parallel because the spatial frequencies of the two gratings are nearly equal. Now, if the two beams can be made to overlap (often by inserting a lens or imaging system) and if they both come from a single light source which has a coherence capability great enough for interference to be possible, then the two beams forming a group will interfere with one another (see Fig. 4). The interference seen is that of two coherent beams impinging on a surface with a slight difference of incidence angle. It is a classic example of two-beam interferometry. For a given wavelength of light, the small angular difference between the two beams is a measure of the spatial-frequency difference between the two gratings. The interference-fringe pattern is a function of this angular difference. The result is an interference pattern indicative of pitch and orientation differences of the two diffraction gratings. In short, it is

the moiré pattern of the two gratings for the area subtended by the incident beam.

Whole-field Analysis

For moiré strain measurement, it is convenient to illuminate the whole field of the two gratings by coherent collimated (usually) light. In this case, there will be a whole field of beams being diffracted by the first grating, and a second field diffracted by the second grating, as pictured in Fig. 5. A field lens is placed in the diffracted beams to decollimate them and to converge them to a focus. In general, the components diffracted at the first grating will focus at a point slightly displaced from the focus of those diffracted at the second grating. If they are close enough to overlap, then an interference pattern is produced. A more useful procedure is to use another lens and screen (that is, a camera) to construct images of the two grating fields with the light contained in the beam groups. Essentially, the camera forms two images which lie on top of one another. Since the image-forming beams are coherent, the two images interfere with one another. The degree of interference depends mainly upon the relative displacement of the two focal spots which, it must be recalled, depends upon the relative inclinations of the sets of beams coming from the diffraction gratings. The image in the camera displays, then, a pattern of interference fringes which are indicative of the local spatial-frequency and orientation differences between the two gratings.

Only minor extensions of these basic ideas suffice to explain the use of moiré gratings in practical measurement situations.

The first complication is that the gratings tend to vary in pitch and orientation from point to point in any strain field of practical interest. One need only apply the reasoning outlined above to each elemental area of the whole field. The result is a set of fringes which vary in direction and spacing from point to point in the field.

The second complication is more difficult to analyze. In general, it is neither wise nor possible to work with
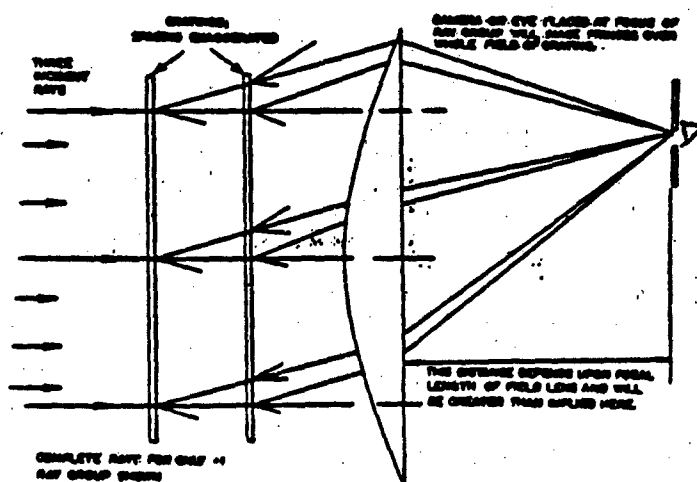

Fig. 5—Diffraction of wide collimated beam by two slim gratings to form whole-field interference pattern

...somewhat gratings. There will exist, therefore, higher order diffractions at each of the two gratings. The number of orders produced from a single beam by each grating depends mainly upon the sharpness of the grating, that is, the degree to which it approaches a rectangular-wave periodic structure. One finds in such a situation that each group of near-parallel beams consists of several individual beams corresponding to different orders of diffraction at each grating. Figure 6 illustrates this behavior. Guild and Post, in the references cited above, considered these more complex cases in considerable detail. For this work, it is sufficient to observe that the basic diffraction and interference concepts still apply. In general, the interference ...at the image will involve more than two component images or beams. In practice, the higher-order diffractions can be attenuated to the point where only the basic two beams in each group are of consequence.

Sensitivity Multiplication

There is one important related fact which holds true if the two gratings are of nearly the same spatial frequency. Each higher-order ray group corresponds to a grating frequency which is a multiple of the basic grating frequency. The image formed by any beam group will form a moiré pattern corresponding to grating frequencies ...

Fig. 6—Diffraction of narrow beam by two bar-space gratings to form ray groups containing higher diffraction orders

Note the following: (1) For simplicity, spatial frequencies of grating C and P are nearly equal; (2) diffraction orders beyond ±2 are not included, and (3) numbers on diffracted rays indicate orders at first and second gratings. C +2, P −1 means diffraction into +2 order at center grating and into −1 order at first grating.
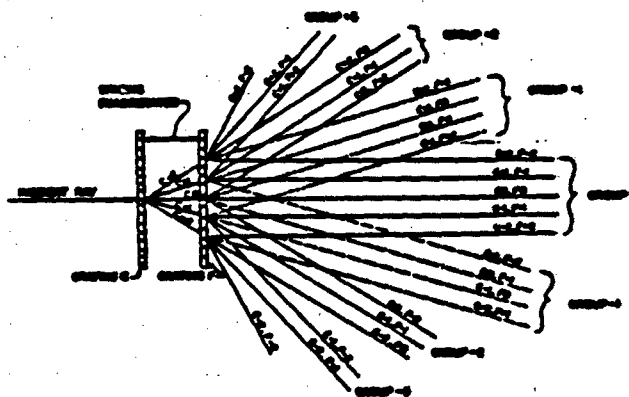

Fig. 7—Diffraction by two gratings, one having spatial frequency three times that of the other

Note the following: (1) Orders beyond ±2 are not included; (2) diffraction angles shown exaggerated; and (3) numbers on diffracted rays indicate orders at first and second grating. P +1, C −2 means diffraction into +1 order at first grating and then into −2 order at center grating.
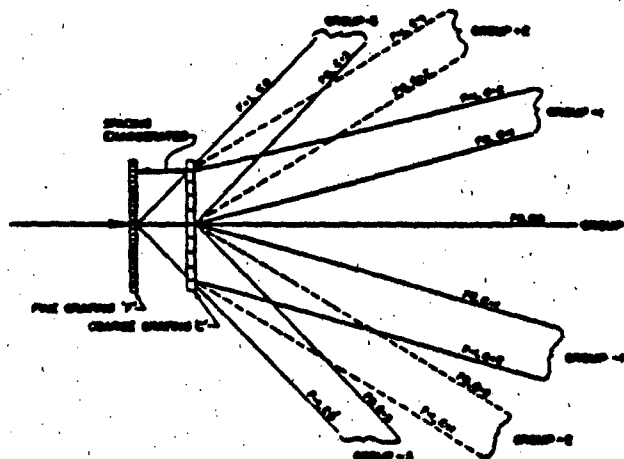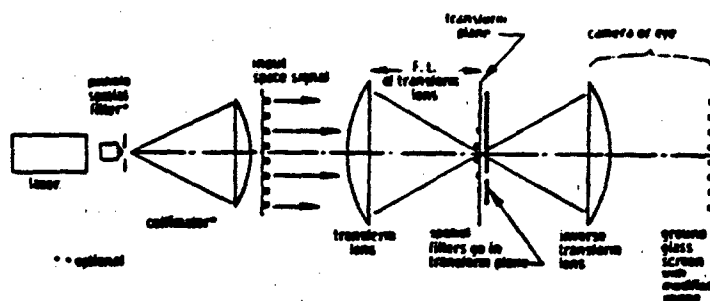
Fig. 6—Optical system for spatial filtering in Fourier-transform plane and creation of inverse transform of modified image

equal to the diffraction order (or group number) times the fundamental specimen-grating frequency. This concept offers a way of multiplying the moiré sensitivity when the two gratings must be of the same base pitch. All one need do is use the light in a higher-order group to form the image and its fringe pattern. Measurement sensitivity is increased by a factor equal to the ray-group number chosen.

A third and very important extension of the basic concepts arises when the gratings are greatly different in spatial frequency; that is, when one grating frequency is a multiple of the other plus a small additional bit which might be imposed deliberately and/or be the quantity which is to be determined. In such a situation, the diffractions are somewhat more complicated, as is the make-up of each of the diffracted-beam groups. Figure 7 illustrates what happens where the second grating frequency is three times the frequency of the first. The basic idea of forming an interference pattern with the rays of a given group still applies; the question arises as to what such an interference pattern means in terms of the frequency and orientation differences between the two gratings. A general interpretation can be very complicated. An important simplification is that, by design and because of the natural attenuation of high diffraction orders, only two of the component rays in any useful ray group will interact to form a visible fringe pattern. Examination of the two main components in, for example, beam-group number 3 in the case pictured in Fig. 7 produces an answer to the interpretation question. These two beams correspond to the first diffraction order at the fine grating and the third order at the coarse grating. The image formed with these two groups will be the same as that which would be produced by two gratings having nearly equal frequencies at three times the fundamental frequency of the coarse grating. The moiré interference fringes in the image will correspond to those which would be produced by two fine gratings. This conclusion is easily supported by careful theoretical analysis. The effects of the remaining beams will be to increase the background noise in the fringe pattern, perhaps to the point of obscuring the moiré fringes.

A striking feature of the situation just discussed is that the moiré-fringe patterns in the camera image are identical, except for background noise and overall brightness, no matter which ray group is used to form the image. It is possible, and good practice, to utilize whichever group gives the best fringe visibility. Stated another way, the sensitivity is not increased by going to a higher diffraction

order, unlike the case when two similar gratings are superimposed.

It is this case where one grating frequency is an integral multiple of the other that has such importance for practical moiré measurement. It allows the use of a coarse specimen grating which is easily applied and photographed. When the grating photograph is superimposed with a finer grating, there appears a moiré-fringe pattern which is the same as that which would be caused by two fine gratings. That is, a coarse specimen grating gives a measurement sensitivity which is equivalent to that of a much finer grating. Post and others have obtained sensitivity multiplications of 20 and 30 in this way. Multiplications of 3 and 4 are easily had with gratings and apparatus of marginal quality.

Optical Transforms and Spatial Filtering

Another approach to understanding the creation of moiré fringes by superimposing specimen and master gratings in a coherent optical system is based on the fact that a simple lens acts as a Fourier transforming device. A very elementary discussion of the concepts behind this technique and examples of its applications are contained in a paper by Cloud. An elegant, readable and comprehensive review of the subject has been written by Vander Lugt. Works by Clark, Durelli and Parks, by Nagas, Iwata and Nagata and by Chiang are representative of the fine papers which have been written about using this concept in strain analysis.

Consider again the situation pictured in Fig. 3, where the light passes through a transparency having a transmission which is a function of the space coordinates. The modulated light beam then passes through a simple lens. There will be produced at the back focal plane of the lens (the focus for the undisturbed light beam) a diffraction pattern which is in essence the square of the amplitude of the Fourier transform of the input signal. If the input is a sinusoidal grating, for example, the transform plane will exhibit three bright patches. The central dot corresponds to the uniform field or 'd-c' component of the input. The other two patches indicate the spatial-frequency content of the input, with radial distance in the transform plane representing spatial frequency on the input plane. If the input signal is a 'square wave' bar and space grating, there will be in the transform plane a row of dots whose positions and brightness indicate the presence and importance of various harmonics of the fundamental space frequency of the input. A two-dimensional grid input will

input signal grid | Fourier transform | filter mask | inverse transform output
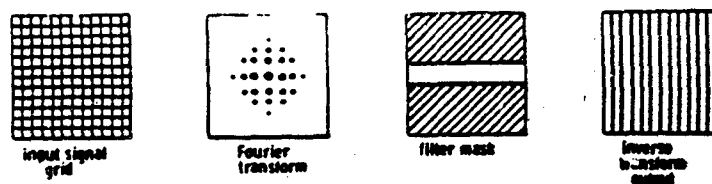
Fig. 9—Example of spatial filtering to create bar grating from a grid

generate a Fourier spectrum at the transform plane which is a two-dimensional array of dots corresponding to the two-dimensional Fourier transform.

Now, if another lens is placed at or near the transform plane, the image of the original input may be cast on a screen. Such a system is shown in Fig. 8. The second lens forms the inverse transform to recover the input. It is possible and often useful, however, to modify the frequency content of the optical image at the Fourier-transform plane before completing the inverse transform. This task can be accomplished by blocking or otherwise changing some portion of the light distribution at the transform plane. Such a procedure is called spatial filtering, coherent optical-data processing, or optical Fourier processing.

A fundamental example of optical Fourier processing is shown in Fig. 9. Here, the input signal is a two-dimensional grid of crossed lines which produces a two-dimensional array of dots at the transform plane. All the dots, except the central vertical row, are blocked by a suitable screen with a slit, which is placed in the transform plane. The inverse transform created by the second lens is found to be a simple grating of vertical parallel lines. The horizontal family of lines is suppressed by the optical filter which has removed all the light required to image the horizontal lines. The potential usefulness of such a process is very great.

In the moiré situation under study here, two superimposed gratings are placed in an optical-data-processing system. A Fourier spectrum of the gratings is created at the transform plane. All but one of the bright patches (actually two or more bright dots close together) are eliminated by a dark mask containing a small hole. The light in this one patch is used by the second lens to form an image on a screen. This lens and screen combination can be an ordinary camera. The image is constructed, then, of light which carries with it information about the periodic structure of the two gratings for whatever fundamental space frequency has been chosen by the placement of the hole. The only rays which get through the hole are those which have been modulated by the gratings at a single space frequency which may be the fundamental grating frequency or one of its harmonics. The image will exhibit moiré fringes which correspond to this space frequency.

A distinctive feature of this approach is that the output image of the gratings is considered to consist of a desirable signal plus a great deal of other information. The important signal is made visible by sifting it from all the extra information. One has a certain latitude in selecting the information that is most useful.

Rationalization of Two Approaches

Having two explanatory models of one process raises

the question of which one is correct—or are both faulty? Actually, the two explanations are not different in basic concept; the difference is one of emphasis. In the diffraction model, we look upon the diversion of portions of the incident beam of light as the important feature. With the Fourier-processing approach, we are concerned with the transfer characteristics of an aperture, which happens to have a lens in it, given an optical signal which is already generated by passing light through a transparency. Of course, the lens would not work correctly if the transparency did not redirect portions of the incident beam by diffraction. This combining and rationalizing of the two approaches could be pursued to a final consistent model. The price for this victory is a small increase in complexity. Further study of the problem would not contribute to the goals of this paper, so it is abandoned with one final observation. As so often is the case with optical processes, the uniting physical phenomenon is that of interference. This property of light is what makes visible for study these minute differences of propagation direction, path length, or wavefront shape which are the physical manifestations of important processes such as diffraction and double refraction.

A Practical Example

An illustration of some of the benefits derivable from simple optical processing of moiré-grating photographs may be drawn from a study of residual-strain fields around coldworked holes by Cloud[18-19]. Only the bare essentials of a typical result can be offered here.

It is in a study of this sort which requires measurement of a broad range of elastic and plastic strain in the presence of out-of-plane displacements that the flexibility of the optical-data-processing procedure becomes useful. The baseline (zero strain) and deformed grating data are permanently stored on glass photographic plates. It is possible to superimpose these plates with each other or with different submaster gratings in order to gain maximum useful sensitivity multiplication and to improve subsequent fringe reading and data analysis by optimizing the spatial-frequency mismatch of the superimposed gratings.

The cold-working strains were measured by printing line and dot gratings of 1000 lpi (39 lines/mm) space frequency onto the specimen surface with Shipley photoresist. The specimen grating was photographed using high-resolution techniques before and after the cold work was imposed. These grating photos were then superimposed in turn with higher-frequency submaster gratings in an optical processor in order to obtain moiré fringes.

The specimen-grating photographs had a spatial frequency of 762 lpi (30 lines/mm) which results with a specimen grating of 1000 lpi magnified 1.3 times. These
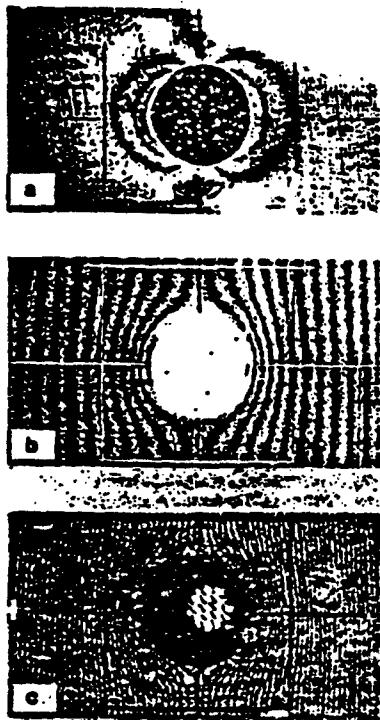
Fig. 10—Typical fringe patterns illustrating some improvements possible with simple optical processing:
(a) From double-exposure grating photo and simple spatial filtering of first order
(b) From specimen-grating photo superimposed with submaster grating of slightly different frequency in optical processor
(c) From specimen-grating photo superimposed with submaster having spatial frequency three times specimen grating plus pitch mismatch

plates could be superimposed with submasters of around 2200 lpi to get a sensitivity multiplication of 3, or of 1542 lpi for a multiplication of 2. An advanced technique, which is mentioned below, gave a multiplication of 4. The various pitch mismatches were chosen to yield the closest fringe spacing obtainable with good fringe visibility. Most grating photoplates were processed with at least three mismatch levels, and sometimes with more than one sensitivity multiplication factor for checking purposes and because it was not possible to assess the quality of a denser fringe pattern through the camera viewfinder, which was used without a magnifier.

To be specific, for most of this study, each baseline photoplate and each data photoplate was superimposed in the processor with submaster grating plates of 2200, 2225 and 2256 lpi. For specimen gratings of poor quality, a sensitivity multiplication of 3 was not practicable and submasters of 1535 and 1492 lpi were used. Some fringe

patterns were made for checking purposes with submasters of 763 lpi. For several of the specimens, all or most of these several moiré patterns were analyzed to gain redundancy of data. This extra information was useful in gaining an appreciation of probable errors and in study of the sensitivity of the data quality to variations in the optical processing.

It was also possible, at this stage, to select parameters which had density and diffraction characteristics which balanced with the properties of the specimen grating replica to produce the best fringe patterns. Also, the ray group which gave best fringe visibility could always be selected.

The 35-mm negatives of the fringe patterns were enlarged and printed in large size for numerical fringe analysis. The ratio of printed image size to specimen size (not negative size) was approximately 7. This magnification plus the moiré sensitivity multiplication and pitch mismatch gave overall sensitivities which were appropriate to the problem.

Some fringe patterns are reproduced in Fig. 10.

Optical Process to Improve Grating Photography

The discussion so far has centered on the treatment of grating transparencies. It is possible to exploit optical processing at the grating photography stage to further simplify procedures and improve results. A particular example is that a slotted aperture mask can be used to tune a photographic system to an integral multiple (including unity) of a grating frequency. Such a procedure is useful for multiplying sensitivity or for obtaining improved rendering of gratings and fringe patterns. Depth of field is increased, and a camera lens of poorer quality than is normally required for high-resolution photography of moiré gratings is adequate. Discussion and examples of such a procedure have been published by Cloud,[14] and details are not repeated here.

References

1. Guild, J., The Interference Systems of Crossed Diffraction Gratings, Clarendon Press Oxford (1956).
2. Post, D., "Analysis of Moiré Fringe Multiplications Phenomena," App. Opt., 6 (11), 1938 (Nov. 1967).
3. Post, D., "New Optical Methods of Moiré-fringe Multiplication," EXPERIMENTAL MECHANICS, 8 (2), 63–68 (Feb. 1968).
4. Post, D., "Moiré Fringe Multiplication with a Non-symmetrical Doubly Blazed Reference Grating," App. Opt., 10 (4), 901 (April 1971).
5. Post, D. and McLaughlin, T.F., "Strain Analysis by Moiré-fringe Multiplication," EXPERIMENTAL MECHANICS, 11 (9), 408–413 (Sept. 1971).
6. Holister, G.S., "Moiré Method of Surface Strain Measurement," The Engineer, 222, 3192, 149 (27 January, 1967).
7. Cloud, G.L., "Lasers in Engineering Education," Eng. Ed., 66 (8), 837 (May 1976).
8. Vander Lugt, A., "A Review of Optical Data-Processing Techniques," Optica Acta, 15 (1), 1–33 (Jan. 1968).
9. Clark, J.A., Durelli, A.J. and Parks, V.J., "Shear and Rotation Moiré Patterns Obtained by Spatial Filtering of Diffraction Patterns," J. Strain Anal., 6 (2), 134 (1971).
10. Nagata, S., Inoue, K. and Noguas, R., "Measurement of Strain Distribution in a Plane Moiré Plate by Optical Spatial Filtering," App. Opt., 14 (1), 113 (Jan. 1975).
11. Chiang, F.P., "Techniques of Optical Spatial Filtering Applied to Processing of Moiré-Fringe Patterns," EXPERIMENTAL MECHANICS, 9 (11), 523–526 (Nov. 1969).
12. Cloud, G.L., Residual Surface Strain in Discontinuous Near Holes which Are Cold-worked to Various Degrees, Air-Force Materials Laboratory, Technical Report AFML-TR-70-153, Wright-Patterson Air Force Base, OH (1970).
13. Cloud, G.L., "Measurement of Strain Near Coldworked Holes," ... 30 (1), 9–16 (Jan. 1980).
14. Cloud, G.L., "Slotted Apertures for Multiplying Grating Frequencies and Sharpening Fringe Patterns in Moiré Photography," Optical Eng., 15 (6), 578–582 (Nov.–Dec. 1976).

APPENDIX D
DISTRIBUTION LIST

This page left blank intentionally.

DISTRIBUTION LIST

CDR   15
Defense Technical Information Center
Bldg. 5 Cameron ANNEX
Attn: DDAC
Alexandria, VA   22314

Manager   2
Defense Logistic Studies
Information Exchange
Attn: AMXMC-D
Ft. Lee, VA   23801

Director
U.S. Army Materials & Mechanics
Research Center
Attn: AMXMR-M   2
      AMXMR-ER   2
      AMXMR-S   2
Watertown, MA   02172

PLASTEC
Picatinny Arsemal
Dover, NJ   07801   1

CDR   1
Air Force Materials Lab
Attn: LTM
Attn: LLN   1
Attn: FIBEC   1
Wright-Patterson AFB, OH 45433

CDR
U.S. Army TACOM
Attn: AMSTA-TSL   2
       AMGTA-R   1
       AMSTA-RCKM   2
       AMGTA-G   1
       AMGTA-CR   1
Warren, MI   48090

Naval Materiel Command   1
Cede CMT0424
Washington, D.C.   20360

Hdq., Dept. of Army   1
Deputy Chief of Staff
For Research, Development and Acquisition
Washington, DC   20310
Attn: DAMA-ARZ-E

CDR
U.S. Army Material Cmd   1
Attn: AMCMT-M
Alexandria, VA   22333

Grumman Aerospace Corp.   1
Bethpage N.Y.   11714
Attn. Mr. Sam Baskin

Dr. Gary Cloud   25
Dept. of Met. Mech. & Mat. Sci.
Michigan State University
East Lansing, MI   48823

Dr. David Sikarskie   25
Dean of Engineering
Michigan Technological University
Houghton, MI   49931